HOKKAIDO UNIVERSITY

Title	Study on the Optoelectronic Properties of Transparent Oxide Semiconductor ASnO3 (A = Ba, Sr, and Ca) Epitaxial Thin Films
Author(s)	,
Citation	. ( ) 14724
Issue Date	2021-09-24
DOI	10.14943/doctoral.k14724
Doc URL	http://hdl.handle.net/2115/83098
Type	theses (doctoral)
File Information	Mian_Wei.pdf

Instructions for use

Study on the optoelectronic properties

of transparent oxide semiconductor ASnO$_3$

(A = Ba, Sr, and Ca) epitaxial thin films

透明酸化物半導体 ASnO$_3$ (A = Ba, Sr, Ca)

エピタキシャル薄膜の光・電子特性に関する研究

Thesis submitted for the completion of Doctor of Philosophy

Mian Wei

Graduate School of Information Science and Technology

Hokkaido University

Table of Contents

List of Figures

List of Tables

List of Acronyms

ADF   Annular dark-field

AFM   Atomic force microscope

CBM   Conduction band minimum

CRT   Cathode-ray-tube

DFT   Density functional theory

DUV   Deep-ultraviolet

GGA   Gradual gradient approximation

HAADF   High-angle annular dark-field

LAADF   Low-angle annular dark-field

LBSO   La-doped $BaSnO_3$

LCD   Liquid crystal display

LCSO   La-doped $CaSnO_3$

LDA   Local density approximation

LED   Light-emitting diode

LSSO   La-doped $SrSnO_3$

OLED   Organic light-emitting diode

PLD   Pulsed laser deposition

RSM   Reciprocal space mappings

STEM   Scanning transmission electron microscope

TCO   Transparent conductive oxide

TFT	Thin film transistor
TOS	Transparent oxide semiconductor
UV	Ultraviolet
UV-VIS	Ultraviolet–visible
UV-VIS-NIR	Ultraviolet-visible-near infrared
VBM	Valence band maximum
XAS	X-ray absorption spectroscopy
XRD	X-ray diffraction
XRR	X-ray reflectivity

List of Symbols

T	Absolute temperature
α	Absorption coefficient
E_a	Activation energy
E_g	Bandgap
k_B	Boltzmann constant
n	Carrier concentration
σ	Conductivity
m^*	Effective mass
F_r	Fermi integral
μ_{FE}	Field effect mobility
φ_{TC}	Figure-of-merit
μ_{Hall}	Hall mobility
D	Lateral grain size
a	Lattice constant
Δa	Lattice mismatch
μ	Mobility
h	Planck constant
ξ	Reduced Fermi energy
r	Scattering parameter
S	Seebeck coefficient

R_s	Sheet resistance
v	Speed of light
ΔT	Temperature difference
ΔV	Thermo-electromotive force
t	Thickness
λ	Wavelength

Chapter 1. General Introduction

1.1 Background of this research

Traditional printing technology, which has more than 100 years of history of being the main way of disseminating knowledge and information, has been replaced by modern display technology. Nowadays, display devices such as television, laptop, and mobile phone are inseparable from people's daily life. According to the pursuit of more colorful pixels and practicality, the display devices have gone through a long journey from cathode-ray-tube (CRT) to plasma display and liquid crystal display (LCD), then to organic light-emitting diode (OLED) [1]. Tremendous amount of research efforts and extraordinary research contributions like the blue LED, which was acknowledged with the Noble prize in 2014 awarded to a trio of Japanese scientists [2], have significantly improved display technology. And the public demand for greater performance eventually created a research discipline called optoelectronics, which refer to electrical technologies associated with controlling light.

For materials to be utilized in optoelectronic applications such as display panels, there are two essential requirements. Firstly, it needs to be transparent to at least allow the visible light to pass through, which enables switching between electrical signal to observable optical signal. In this regard, the material needs to have a relatively wide bandgap. In

addition, materials in display technology are required to exhibit high electrical properties. *i.e.,* high conductivity for reducing the power consumption and high mobility for ensuring the fast performance. In these regards, two essential class of materials in optoelectronics are transparent conductive oxides (TCOs), which is used as electrodes for the optoelectronic devices, and the transparent oxide semiconductors (TOSs), which is applied for channel materials of the transistor consisting the various applications [3].

The pioneering research work on transparent conductive materials began when military scientists started to use transparent oxides for deicing window glass for aircrafts during World War II. In 1950, the transparent semiconductor oxide In_2O_3 was made for the first time [4], and scientists soon realized that adding tin (Sn) in In_2O_3 made this material system an excellent conductor, which could be used as transparent conductive films. If Sn is doped in In_2O_3, Sn replaces In in the lattice and contributes an electron to the conduction band since In in In_2O_3 is trivalent. In addition, oxygen vacancy can be generated, and the resulting electrical transport properties of this material system can be a carrier concentration of ~ 10^{21} cm^{-3} and a mobility of ~ 40 cm^2 v^{-1} s^{-1} [5]. This mechanism provides ITO an excellent electrical conductivity ~10000 S cm^{-1} [5], and commercial ITO films are widely used for the electrode for most optoelectrical devices. However, for optoelectronic devices used in ultraviolet (UV) or deep-ultraviolet (DUV) range, UV-LED for example, due to the limitation of ITO's relatively narrow bandgap, the efficiency of the UV light transmission is relatively low. Moreover, the use of In

comes with practical cost issues due to its low abundance [6], which will limit the economic viability of using ITO in large-scale optoelectrical devices like flat panel display and solar cell. Therefore, many researchers are working on finding an alternative optoelectronic material that can potentially replace ITO.

The relationship between bandgap and conductivity can be tricky since these two physical properties are usually mutually exclusive. As an electrode is an electrical conductor used to contact nonmetallic part of a circuit, materials with high electrical conductivity are preferred. Almost all metals exhibit sufficient electrical conductivity because of the free electron gas, but these free electrons form a sea of electrons called plasma, which can effectively reflect electromagnetic waves. As such, metal exhibits excellent electrical conductivity and is opaque without a bandgap. This trade-off relationship between the bandgap and electrical transport properties is very important in optoelectronics application, and such requirements can be met with TOSs.

High carrier mobility is another essential requirement for optoelectronic applications. For flat panel displays in commercial applications like LCD, OLED, and LED, each pixel is individually controlled by thin film transistors (TFTs), and the speed of charge carriers is essential for their performance. Metaphorically speaking, the carrier mobility, which is associated with the drift speed of charge carriers, is analogous to the speed of a train. If the train speed is slow, in order to transport a certain amount of goods within a specified

3

time, multiple rails or additional carriages are required. Similarly, if the carrier mobility

of the channel is high, each transistor can be made smaller, and each pixel can be made

smaller to achieve higher display resolution. In order to ensure fast performance of TFTs,

high carrier mobility value of their TOS channels is critical. Conventional display panels

during the early era utilized Si and SiO_2 as the backplane and channel materials, of which

the main benefits were extremely low cost and easy synthesis. However, the mobility

value of amorphous-Si (a-Si) based TFTs is < 1 cm^2 v^{-1} s^{-1} [7]. The research efforts to find

materials with better performance eventually led to the development amorphous

$InGaZnO_4$ (IGZO). IGZO currently dominates the market as a channel material in the

new generation of high-performance TFT to improve the resolution of display panels in

large-screen OLED TVs [8] due to its many advantages. It is transparent, and the

amorphous IGZO (a-IGZO) based TFT shows a mobility value around 10 cm^2 v^{-1} s^{-1},

which is two orders of magnitude higher than that of a-Si. However, some issues still

remain. For example, it still contains In, which is not abundant [6].

Widely used TCOs and TOSs are not limited to ITO (bandgap, E_g 3.50~3.65 eV, ~10000

S cm^{-1}) [5] and a-IGZO (E_g ~3 eV, ~400 S cm^{-1}) [9]. For cost reduction and concerns

related to preserving the environment, zinc oxide (ZnO) is considered as a candidate since

it includes no rare elements. Al-doped and Ga-doped ZnO thin films show a conductivity

of ~5000 S cm^{-1}, which is only half of that in ITO [10, 11]. Moreover, since Zn is more

reactive than Sn and In under oxygen atmosphere, controlling the Zn content during

synthesis is more difficult than other commercialized TOSs, limiting the use of ZnO in optoelectrical applications. As another alternative, tin oxide (SnO_2) based TFT shows extremely high field effect mobility (μ_{FE}) >100 cm^2 V^{-1} s^{-1} [12, 13], which is one order of magnitude higher than that of a-IGZO. In 2016, Shin *et al.* reported that an extremely thin (< 4.5 nm) undoped SnO_2 TFT exhibited μ_{FE} of 150 cm^2 V^{-1} s^{-1} at room temperature in air [13]. However. SnO_2 is a well-known gas sensor material [14]. It is known that a 3−4-nm-thick depletion layer is formed at the SnO_2 surface [15]. Oxygen in the aerial atmosphere is adsorbed on the surface and seizes some free electrons near the surface, forming a depletion layer. The consequent sensitivity to temperature and humidity limits practical application of SnO_2.

There are also attempts to expand the range of transparency to Deep-UV (DUV, 200−300 nm in wavelength) for next generation optoelectronic applications [16]. One promising application area of interest is biotechnology since DNA molecules have characteristic absorption and fluorescence in DUV region [17, 18]. DUV light is also used for sterilization and cleaning, which require efficient UV-LED. Room temperature operation of DUV laser diode (271.8 nm) was developed by Zhang *et al.*, [19] which can be utilized in integrated lithography in a large scale and high-density optical memories.

Candidate TOS materials for DUV optoelectronics include β-Ga_2O_3 (E_g ~4.9 eV, ~1 S cm^{-1}) [20, 21], α-Ga_2O_3 (E_g ~5.3 eV, ~0.3 S cm^{-1}) [22], electron-doped calcium aluminate

(C12A7:e^-, ~4 eV, ~800 S cm^{-1}) [23-25].β-Ga$_2$O$_3$ recently emerged to be a potential candidate for DUV optoelectronics [26, 27]. Although theoretical studies predict that carrier doping in β-Ga$_2$O$_3$ is challenging, [28] experimentalists successfully created mobile electrons using Sn or Si dopants [29, 30]. However, the resulting electrical conductivity was too low for (<30 S cm^{-1}) practical applications. Al doped MgZnO (AMZO) is another candidate. Undoped MgZnO (MZO) itself is a promising candidate for DUV applications due to its economic advantages [31, 32], but its UV transmittance can further be improved by adjusting the Mg content while carriers can be doped with Al, Ga or In [33, 34]. Al doped Mg$_{0.43}$Zn$_{0.57}$O (AMZO) film with a wide bandgap (cutoff wavelength of 295 nm), high carrier concentration (1.56×10^{20} cm^{-3}), high mobility (16.3 cm^2 V^{-1} s^{-1}), and high conductivity (406.6 S cm^{-1}) has been reported by D. Zhang *et al* [35]. However, due to the tradeoff relationship between the optical bandgap and the electrical conductivity, DUV-TOSs exhibit low electron mobilities, and the resulitng electrical conductivities are too low compared to conventional ITO electrodes.

The search for better material system is the duty of material scientists. In this regard, one promising TOS for future optoelectronic applications is the Alkaline earth elements stannate, ASnO$_3$. ASnO$_3$ has perovskite structure composed of corner-sharing SnO$_6$ octahedra with the A-site cations. The crystal structure of ASnO$_3$ is closely related to lattice parameter, which is determined by A-site substitution. The smaller A-site cation with stronger binding force of nucleus trigger the deformations in the SnO$_6$ octahedral

and further induce phase transition in ASnO$_3$. The valence band maximum (VBM) and

conduction band minimum (CBM) of ASnO$_3$ is composed of O 2p and Sn 5s, respectively,

and the energy location of the CBM and VBM is affected by the Sn–O bond length,

enabling the A-site modulation to control all optical and electrical properties. Therefore,

this system could achieve a good trade-off relationship between electrical transport

properties and optical bandgap at the same time by changing the A-site ions.

La-doped ASnO$_3$ (A = Ba, Sr, and Ca) is a rapidly emerging material class for

optoelectronics application, as they have both the wide bandgap and fast electrical

transport properties. There has been growing interest on La-doped BaSnO$_3$ (LBSO,

bandgap, $E_g \sim 3.5$ eV) with cubic perovskite structure ($a = 4.115$ Å) as a novel TOS

because flux-grown LBSO single crystals exhibited a very high mobility of 320 cm^2 V^{-1}

s^{-1} with a carrier concentration value of 8×10^{19} cm^{-3}) at room temperature [36].

Therefore, many researchers have tried to prepare high mobility LBSO epitaxial films to

date, but the observed mobility has been low compared to that of single crystals. Paik *et*

al. obtained the highest mobility of 183 cm^2 V^{-1} s^{-1} in a LBSO film on DyScO$_3$ ($a = 3.943$

Å, $\Delta a = +4.2$ %) [37]. and Raghavan *et al.* also achieved high mobilities of 150 cm^2 V^{-1}

s^{-1} and 100 cm^2 V^{-1} s^{-1} in LBSO films deposited by high purity molecular beam epitaxy

(MBE) technique on PrScO$_3$ ($a = 4.026$ Å, $\Delta a = +2.18$ %) and SrTiO$_3$, respectively [38].

Higgins *et al.* reported mobility values up to 81 cm^2 V^{-1} s^{-1} in LBSO films grown on

TbScO$_3$ (110) ($a = 3.958$ Å, $\Delta a = +3.97$ %) by MBE [39]. A low mobility value of 10 cm^2

V^{-1} s^{-1} was also reported by Wadekar *et al.* in a LBSO film on $SmScO_3$ (110) ($a = 3.991$ Å, $\Delta a = +3.1$ %) [40]. The origin of this mobility suppression must be clarified to utilize the high mobility in LBSO for device applications, but it is currently under an extensive debate.

Replacing Ba in LBSO with Sr can enhance the bandgap from 3.1 eV to > 4 eV [41-44]. However, the substitution of Sr induces lattice distortions and reduces the electron mobility. Therefore, La-doped $SrSnO_3$ (LSSO) is not studied as extensively as LBSO. The crystal structure of $SrSnO_3$ is regarded as a pseudo-double cubic perovskite though the real lattice is orthorhombic [41]. Several researchers fabricated the epitaxial films of LSSO using vapor phase epitaxy methods. However, due to difficulties in growing high-quality LSSO films, their electron transport properties have not been extensively studied. One study reported the electrical conductivity of 5% La-doped LSSO film only to be ~1000 S cm^{-1} with a low activation rate of La, which is the highest electrical conductivity reported to date [45]. However, the large bandgap enhanement observed from LSSO is worth dedicated studies due to its potential in DUV applications. The electrical conductivity of LSSO films can be improved if the solubility of La ions in the LSSO lattice is enhanced.

The trend observed from LBSO and LSSO suggests that reducing the *A*-site ion size increases the bandgap. Therefore, the optical bandgap of $CaSnO_3$ is of interest to the

optoelectronics community, but the reported values are scattered from 1.95 to 5.38 eV. [46-48] Using first principle calculations based on the density functional theory (DFT), Cherrad *et al.* reported a bandgap value of 2.849 eV [49], and Henriques *et al.* reported 1.95 eV (2.92 eV), which was estimated with gradual gradient approximation (local density approximation) (GGA (LDA)) for orthorhombic $CaSnO_3$ [50]. Zhang *et al.* experimentally reported ~4.44 eV from the UV-VIS absorption spectra and Raman spectroscopy, but this result contradicted their own DFT result of ~2.5 eV [51]. Mizoguchi *et al.* reported an optical bandgap of ~4.4 eV from $CaSnO_3$ compounds [42]. Liu *et al.* reported the optical bandgap of $CaSnO_3$ thin film grown on LAO. The bandgap gradually increased from 4.95 eV to 5.38 eV with decreasing film thickness, which they attributed to the quantum-size effect [48]. The electrical properties of $CaSnO_3$ has not been addressed in literature to date.

1.2 Objectives of this research

The objective of this research is to develop high-performance TOS, ASnO$_3$ by optimizing the physical properties and fabrication process. This thesis is divided into the following chapters. In chapter 1, the overall research is introduced with the background and motivation. The experimental methods including films fabrication, structural characterizations and electron transport properties are explained in chapter 2. In chapter 3-5, improving the electron transport properties and optimizing the fabrication process of LBSO and LSSO are discussed in detail. Efforts to clarify the origin of the mobility suppression in of LBSO thin films mobility have been made, and several methods have been tested, such as using an oxidate atmosphere during films growth and vacuum post-annealing to further optimize the performance. As the results, higher activation efficiency of La-dopant was achieved, and the electrical properties of LBSO and LSSO were greatly improved. In chapter 6, the research was expanded to general ASnO$_3$ system, and its optoelectronic properties were systemically clarified. The overall trade-off relationship with the substitutions of different A-site ions in the optoelectronic properties in this material system was demonstrated. The overall research results and recommendations for future research are summarized in chapter 7. The contributions reported in this dissertation will be of great importance in the design of the next-generation optoelectrical applications based on ASnO$_3$.

Chapter 2. Experimental Methods

2.1 Film fabrication

In this research, epitaxial ASnO$_3$ thin films were fabricated on various single crystal substrates using pulsed laser deposition (PLD) technique (KrF excimer laser, λ=248 nm, 10 Hz, fluence ~2 J cm^{-2} pulse^{-1}), which is one of physical vapor deposition methods. [53] **Figure 2.1** shows the schematic illustration of the PLD system. The PLD equipment largely consist of an excimer laser and a high-vacuum chamber. At the start of deposition, pulsed laser with high power will be directed to the target by mirrors to ablate the surface. This process can occur under ultra-high vacuum or the presence of background gas such as oxygen. As shown in **Figure 2.2**, when the laser pulse is absorbed by target, the laser energy will first be converted to electronic excitation and then into thermal excitation, resulting in plasma formation [54]. The plasma expands to the surrounding environment in the form of a plume containing many energetic target particulates at atomic level, including atoms, electrons, and ions [55]. Then they will be deposited on the substrate. Sometimes, the substrate needs to be heated to a specific temperature for growing high-quality films.

Compared to other film deposition methods, PLD can fabricate thin films with the same chemical composition as the target, which is crucial in this research for controlling the

composition in the ASnO$_3$ films. The PLD process also enables the deposition of films in a wide range of background gas compositions and pressures, which is ideal for the studying the effect of atmospheric conditions during the film deposition [50]. In order to create a higher oxidative environment and control the chemical potential of oxygen during the film growth, ozone (O$_3$) was used for film grown atmosphere in this research. O$_3$ creates a much stronger oxidation environment compared to typically used oxygen gas (O$_2$). The ozone generator is shown in **Figure 2.3**. The ozone generating unit in the generator converts flowing oxygen gas into a mixture of oxygen and ozone in the gap of double quartz glass tube.

2.2 Structural characterization

High-resolution X-ray diffraction (XRD) (**Figure 2.4**, Cu, Kα_1, ATX-G, Rigaku Co.) measurements were used to reveal the crystal structure and other physical properties of films associated with the structure. The basic principle of XRD is expressed by the Bragg's law:

$$2dsin\theta = n\lambda$$

As shown in **Figure 2.5**, the incident wave can be scattered by atoms, which reflect a small portion of the incident intensity. If the atoms are arranged symmetrically on planes with a separation d, these waves will be in constructive interference only at certain angles (θ) when their path-length difference, $2d\ sin\ \theta$, equals an integer multiple (n) of the

wavelength λ. In this case, the incident beam is deflected by an angle 2θ, producing a peak in the diffraction pattern [53]. X-ray reflectivity (XRR) contains the information from the thickness and density of thin films, which is based on the oscillation pattern from the interference of reflected beam at the film/substrate interface and film surface [54]. The film thicknesses were determined by analyzing Kiessing or Pendellöesung fringes. In addition, it can check if the film was heteroepitaxially grown on substrates.

In order to address the structural characteristics in more detail, X-ray reciprocal space mappings (RSMs) were performed. Compared to the conventional out-of-plane XRDs, additional information like the lattice relaxation and the crystalline quality can be extracted from RSMs [55]. The lattice parameters perpendicular (c-axis) and parallel (a-axis) to the substrate surface can also be extracted from the peak position since RSM can be seen as the 2D XRD patterns of films along the in-plane and out-of-plane directions. Lastly, the lateral grain size value can be calculated from the peak width.

The surface morphology of the films was investigated using an atomic force microscope (**Figure 2.6**, AFM, Nanocute, Hitachi High-Tech Sci. Co.). The surface profile is collected by a sharp probe on a micro-cantilever, which is controlled precisely with a piezoelectric crystal. The conductive cantilever and AFM measure the current bias of the sample, then sense and amplify the signal between the probe and the atom on the sample surface with resolutions on the order of a few tens of nanometers.

In order to determine the atomic structure of the interface between film and substrate, the ASnO$_3$ films was characterized by annular dark-field (ADF) imaging in a scanning transmission electron microscope (STEM), of which the images are formed by collecting scattered electrons with an ADF detector. From high-angle annular dark-field (HAADF) STEM images, individual atoms can be identified. Since the HAADF-STEM image are formed only by incoherently scattered electrons at high angles (Rutherford scattered from the nucleus of the atoms), it is highly sensitive to variations in the atomic number of atoms in the sample (Z-contrast images). As such, atomic level defects like misfit dislocations can be observed. Strain contrast in the films were observed in the cross-sectional low-angle annular dark-field (LAADF)-STEM images, which collects diffracted or inelastically scattered electrons at low to medium angles using the ADF detector. LAADF-STEM enables the acquisition of a high-resolution image with a high signal-to-noise ratio, of which the intensity depends on the lattice strain.

2.3 Electron transport properties

The electron transport properties, such as Hall mobility (μ_{Hall}), carrier concentration (n), and electrical conductivity (σ) of the ASnO$_3$ films were measured using the conventional DC four-probe method with the van der Pauw electrode configuration. In-Ga alloy was used as the contact electrode. In order to measure the Seebeck coefficient (S) of the films,

two Peltier devices were used to provide a temperature difference between source and drain electrodes, and the thermo-electromotive force (ΔV) and temperature difference (ΔT) were monitored simultaneously (**Figure 2.7**). The S values were obtained from the slope of the ΔV-ΔT plots.

2.4 X-ray absorption spectroscopy

X-ray absorption spectroscopy (XAS, **Figure 2.8**) is a widely used technique for determining the local electronic state of the atoms in a substance. As the X-ray goes through the sample, its intensity attenuates, which is closely related to the structure and composition of the sample. Since the attenuation comes from the sample's absorption and scattering of X-rays, but the effect of absorption is much greater than that of scattering. The X-ray absorption is related to the atomic number and valence, which can be used for the composition as well as the valence state of the material constituents. In order to investigate the chemical state of the ASnO$_3$ films, XAS is performed around the Sn M4,5 edge of LBSO film.

2.5 Optical properties

The optical bandgap of the films was calculated using the optical transmission and reflectance measured by the ultraviolet-visible-near infrared (UV-VIS-NIR) spectrometer (**Figure 2.9**). A beam is separably divided into its constituent wavelengths by a prism,

and each monochromatic (single wavelength) beam is divided into two beams of equal

intensity by the half mirror device. One beam (sample beam) passes through the sample

to be tested, and the other beam (reference beam) passes through only the substrate. The

electronic detector measures the intensity of the beams and compares them to yield the

optical properties of the films.
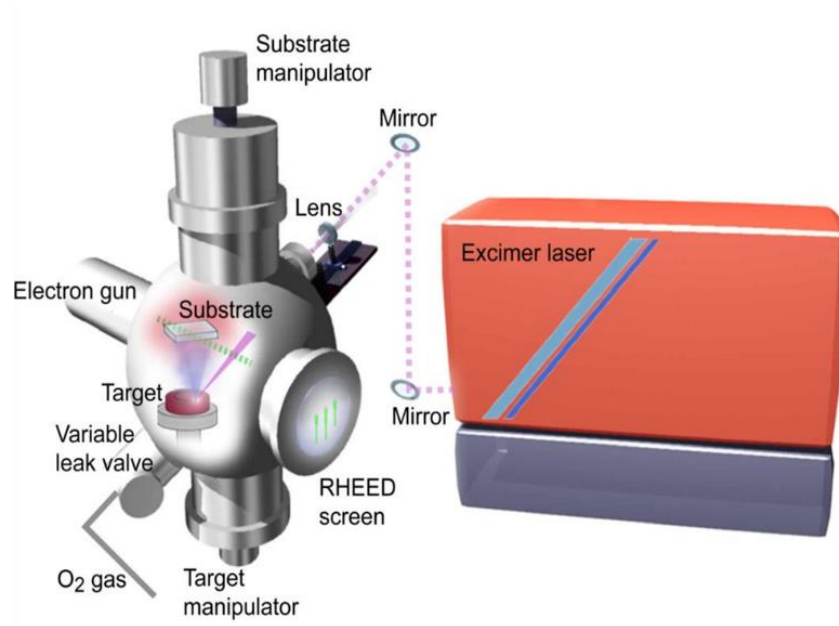
Figure 2.1 Schematic illustration of PLD system.

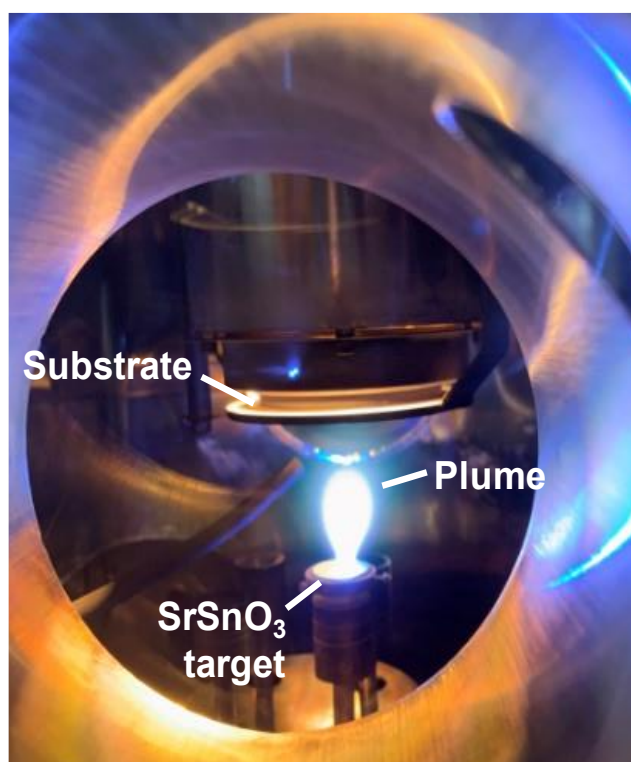**Figure 2.2 Plasma created by pulsed laser during the deposition of SrSnO₃ films.**

Figure 2.3 Ozone generator.
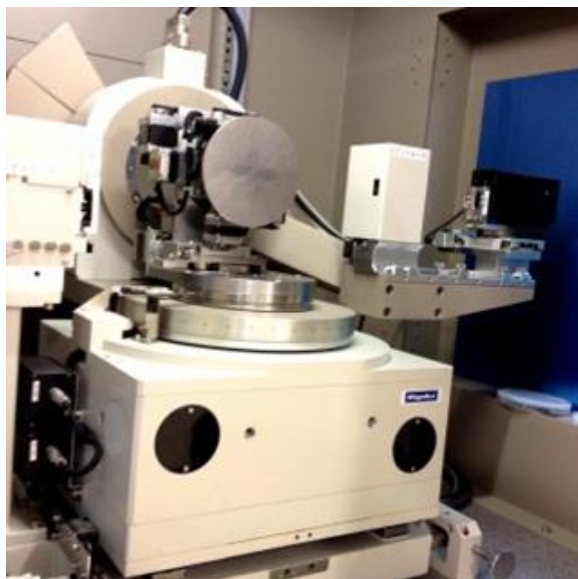
Figure 2.4 High-resolution XRD.
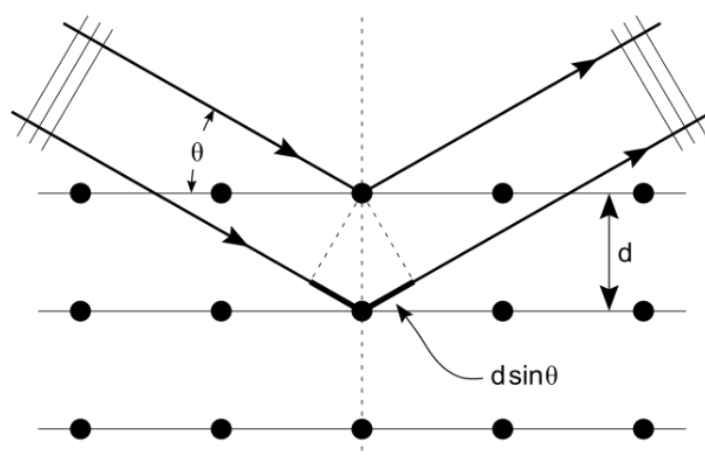
Figure 2.5 Schematic illustration of Bragg's law.

Figure 2.6 AFM.
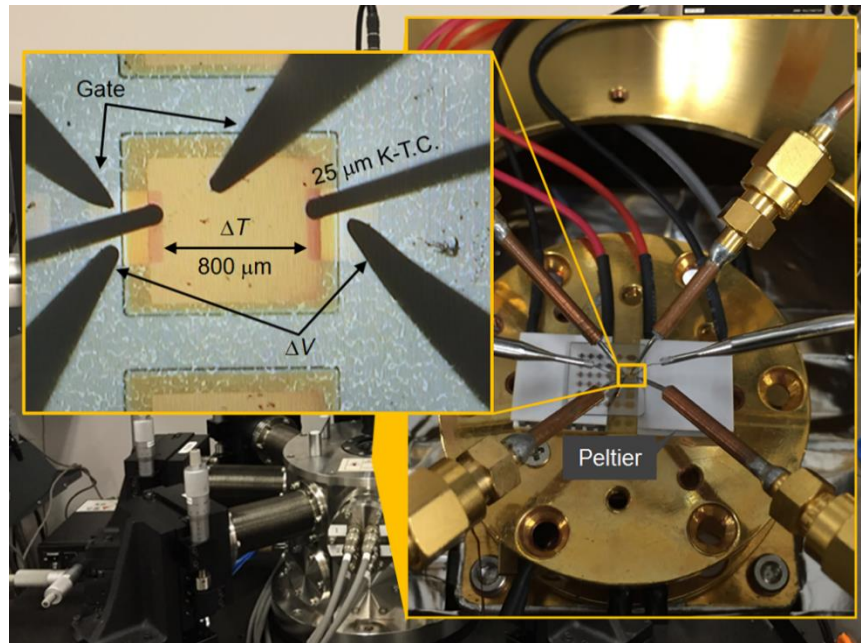
Figure 2.7 Four-probe electron transport property and thermopower measurements.
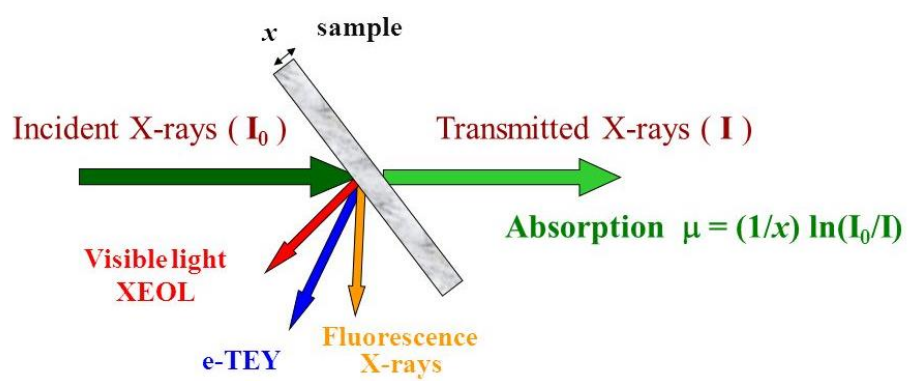
Figure 2.8 Schematic diagram of XAS measurements.

25

Figure 2.9 UV-VIS-NIR spectrometer.

Chapter 3. Large Thickness Dependence of the Carrier Mobility in a Transparent Oxide Semiconductor, La-doped BaSnO₃

3.1 Objective of this chapter

LBSO single crystals exhibits an extraordinarily high mobility of 320 cm^2 V^{-1} s^{-1} ($n \sim 8 \times 10^{19}$ cm^{-3}) at room temperature [36], which is even comparable to classical semiconductors. Such high mobility is originated from its small carrier effective mass (m^* = 0.40 m_e [56]) and long carrier relaxation time [57]. For this reason, many researchers attempted to prepare LBSO epitaxial films on various substrate, but the resulting electron mobility values vary in the range of 10−183 cm^2 V^{-1} s^{-1} at room temperature. These studies attributed the origin of the low mobility to the misfit/threading dislocations, which are generated from a large lattice mismatch (Δa) at the film/substrate interface (*i.e.,* Δa = +5.4 % for LBSO/SrTiO₃ interface) [58-61]. In order to minimize Δa, various forms of buffer layers, even including BaSnO₃, were implemented, but the resulting mobilities were still lower than 100 cm^2 V^{-1} s^{-1}. These contradict the misfit/threading dislocations scenario since there was almost no lattice mismatch between the substrate and the film, especially for BaSnO₃ substrates.

Several studies suggest that cation off-stoichiometry or cation mixing can introduce

charge point defects and dislocations [62-64], which may act as scattering sources and thus suppress the mobility. Due to the existence of many possibilities, the origin of the limited electron mobility in LBSO thin films has not been clearly explained to date, and a fundamental study on other simple factors such as the film thickness is required to understand this phenomenon. Therefore, in this chapter, the structural and electrical features of epitaxial LBSO films with various thicknesses (14−1040 nm), which were grown on (001) perovskite $SrTiO_3$ (Δa = +5.4 %) and non-perovskite (001) MgO (Δa = −2.3 %), were analyzed.

This chapter demonstrates that the carrier mobility of the LBSO films strongly depends on the thickness whereas it is unrelated to the lattice mismatch. Despite the large observed differences in lattice parameters, lateral grain size, density of threading dislocations, surface morphology, and density of misfit dislocations, the mobility increased very similarly with the thickness on both substrates and saturated at ~100 cm^2 V^{-1} s^{-1} while approaching to the nominal carrier concentration (= [2% La^{3+}]), clearly indicating that the behavior of mobility depends on the film thickness.

3.2 Experimental

Epitaxial 2% LBSO films with thicknesses varying from 14 nm to 1.04 μm were heteroepitaxially grown on (001) $SrTiO_3$ and (001) MgO single crystal substrates using

PLD. The temperatures during the film growth were 700 °C for $SrTiO_3$ substrates and 750 °C for MgO substrates while the oxygen pressure was kept at 10 Pa. In case of $SrTiO_3$ substrates, the LBSO films were annealed at 1200 °C in the air to obtain atomically smooth surfaces [56, 65].

3.3 Results and Discussion

High-resolution XRD measurements revealed that the LBSO films were heteroepitaxially grown on (001) $SrTiO_3$ substrates and (001) MgO substrates with a cube-on-cube epitaxial relationship. For very thick films, Pendelloesung fringes were used to determine the thickness. **Figure 3.1** shows the observed stepped and terraced surface on the film grown on (001) $SrTiO_3$ substrate, whereas very tiny grains were observed from the film grown on (001) MgO substrate. The AFM images show that the films grown on $SrTiO_3$ and MgO have very different surface morphologies.

Figure 3.2 shows the X-ray RSMs performed around the asymmetric 103 diffraction spot of $BaSnO_3$ with the 103 diffraction spot of $SrTiO_3$ and the 204 diffraction spot of MgO, respectively. While the $q_x/2\pi$ peak position of $BaSnO_3$ and the substrate are different from each other, they are both located nearby the red dotted line (cubic), indicating that incoherent epitaxial growth occurred in both cases. In order to determine the lateral grain size (D), the cross-sectional peak intensity as a function of $q_x/2\pi$ was plotted. In the case

of SrTiO$_3$ substrate, an integral width of 0.0306 nm^{-1} was obtained for the 14-nm-thick

film whereas that of 0.0127 nm^{-1} was obtained for the 1040-nm-thick film. In the case of

MgO substrate, an integral width of 0.1085 nm^{-1} was obtained for the 44-nm-thick film

whereas that of 0.0557 nm^{-1} was obtained for the 1000-nm-thick film.

Figure 3.3 (a) shows the calculated average lattice parameters, $(a^2 \cdot c)^{1/3}$ of the LBSO films

grown on SrTiO$_3$ and MgO substrates, where a and c are the in-plane and the out-of-plane

lattice parameters, respectively. The $(a^2 \cdot c)^{1/3}$ values of the films on SrTiO$_3$ and MgO

substrates initially showed opposite behaviors; $(a^2 \cdot c)^{1/3}$ of the films on MgO was larger

than the bulk value whereas that of the films on SrTiO$_3$ was smaller than the bulk value,

which are probably attributed to the differences in the lattice mismatch. On both

substrates, the $(a^2 \cdot c)^{1/3}$ values were nearly similar when the thickness was greater than

300 nm. The lateral grain size (D = [integral width in $q_x/2\pi$ direction of the RSM]$^{-1}$) of

the LBSO films grown on SrTiO$_3$ and MgO substrates were calculated, which are shown

in **Figure 3.3 (b)**. The lateral grain sizes were quite different as the LBSO films on SrTiO$_3$

exhibited a maximum grain size of ~85 nm whereas the grains in the LBSO films on MgO

were 20 nm or less.

Figure 3.4 shows the cross-sectional HAADF-STEM images of the 1.04-µm-thick

LBSO/SrTiO$_3$ and 1-µm-thick LBSO/MgO films. In case of LBSO/SrTiO$_3$, mismatch

dislocations (indicated by arrows) are observed periodically at the interface. The spacing

of the mismatch dislocation was about 7.3 nm, which agrees with the Δa = +5.3 %. On the other hand, in case of LBSO/MgO, mismatch dislocations were not periodically spaced. Highly dense threading dislocations were observed in the cross-sectional LAADF-STEM images of the films as shown in **Figure 3.5**. The average distance between two threading dislocations was ~100 nm on SrTiO₃ substrate and ~30 nm on MgO substrate, reflecting the lateral grain sizes obtained from the RSMs (~85 nm for SrTiO₃ substrate and ~20 nm for MgO substrate). Thus, the densities of the threading dislocations are 1.4×10^{10} cm^{-2} for the film on SrTiO₃ substrate and 2.5×10^{11} cm^{-2} for the film on MgO substrate. These results show that there are several structural differences between the LBSO films on SrTiO₃ and MgO substrates, including surface morphology, lattice parameter, lateral grain size, density of threading dislocations, and density of misfit dislocations.

Figure 3.6 summarizes the electron transport properties of the LBSO films grown on SrTiO₃ and MgO substrates at room temperature. As far as the overall tendencies are concerned, no clear difference was observed from LBSO films deposited on SrTiO₃ and MgO substrates. The value of n increased with increasing thickness and approached the nominal carrier concentration (= [2% La^{3+}]). Approximately, 88 % La^{3+} dopants were activated and produced conducting electrons for films thicker than 350 nm. Similarly, as shown in **Figure 3.6 (b)** the magnitude of S, which decreases with increasing n, gradually decreased with the thickness, which is consistent with **Figure 3.6 (a)**. All values of S were

negative, indicating the LBSO films are *n*-type semiconductors [66]. In addition, μ_{Hall}

increased gradually with thickness and became constant for films thicker than 350 nm.

The highest mobility values were 97.7 $\text{cm}^2 \text{ V}^{-1} \text{ s}^{-1}$ for 1040 nm thick LBSO/SrTiO₃ and

99.2 $\text{cm}^2 \text{ V}^{-1} \text{ s}^{-1}$ for 450 nm thick LBSO/MgO. The thickness dependence of μ_{Hall} and *n*

in the LBSO films were similar on both the SrTiO₃ and MgO substrates. In addition, since

μ_{Hall} and *n* of LBSO films thicker than 350 nm do not show a significant dependence on

the substrates, the contributions from the structural differences between LBSO/SrTiO₃

and LBSO/MgO on the mobility are likely small.

The electron mobility in LBSO films rapidly increased with the thickness. However, the

maximum mobility (~100 $\text{cm}^2 \text{ V}^{-1} \text{ s}^{-1}$) was still low compared to the bulk values (~320

$\text{cm}^2 \text{ V}^{-1} \text{ s}^{-1}$). In order to further investigate the suppression of electronic transport

properties, XAS was performed around the Sn $M_{4,5}$ edge of a 500-nm-thick LBSO film

on SrTiO₃ substrate in Pohang accelerator laboratory as shown in **Figure 3.7**. Several

peak structures (A–F) were clearly observed in the XAS spectra. The peaks labelled as

B–F are well matched with BaSnO₃. However, there is an additional peak from 2+ valence

state of Sn (SnO, peak A). Since Sn^{2+} ions in LBSO films should play as electron

acceptors as well as ionized impurities, they may be related to the suppression of μ_{Hall} and

n in the films (compared to bulk values).

Figure 3.8 shows the measured the temperature dependence of the electron transport

properties of the LBSO films grown on (001) SrTiO₃ substrates. Metallic behavior was observed in all the films as shown in **Figure 3.8 (a)**, indicating that the Fermi energy is located above the conduction band edge and the films behave as degenerate semiconductors [61]. The values of *n* for all films shown in **Figure 3.8 (b)** were almost temperature independent and similar for films thicker than 350 nm. μ_{Hall} increased with decreasing temperature, and the change was more significant for thicker films. The highest μ_{Hall} of 163 cm^2 V^{-1} s^{-1} was observed in 1040 nm thick LBSO film at 8 K (**Figure 3.8 (c)**). |*S*| almost linearly decreased with decreasing temperature (**Figure 3.8 (d)**), which is typical for degenerate semiconductors [66].

3.4 Conclusions

This chapter demonstrated that the electron transport properties of the LBSO films grown on (001) SrTiO₃ and (001) MgO substrates show strong thickness dependence in the range of 14 nm to 1040 nm. Although the LBSO/SrTiO₃ and LBSO/MgO exhibited several drastic structural differences, these discrepancies did not play a major role in the carrier mobility as no clear structure-originated difference was observed in the electron transport properties. μ_{Hall} and *n* increased with increasing LBSO film thickness. On both SrTiO₃ and MgO substrates, the maximum μ_{Hall} observed was ~100 cm^2 V^{-1} s^{-1}. While the origin of the strong thickness dependence of μ_{Hall} remains unclear, the presence of 2+ valence state of Sn in the XAS spectrum of a 500 nm thick LBSO film offers on insight. Since

Sn^{2+} ions should be electron acceptors as well as ionized impurities, they may increase

the scattering cross section of the electrons and contribute to the mobility suppression.

These results can provide a guideline for the thickness optimization of high-mobility

LBSO films grown on other substrates and further insights on the development of LBSO-

based electronic devices.
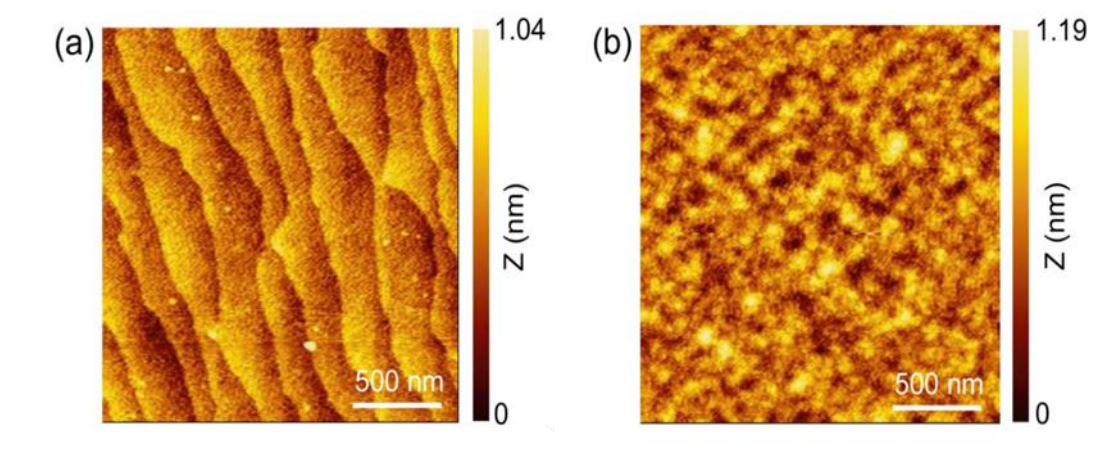
Figure 3.1 Topographic AFM images of the LBSO films grown on (a) (001) SrTiO₃ and (b) (001) MgO substrates.
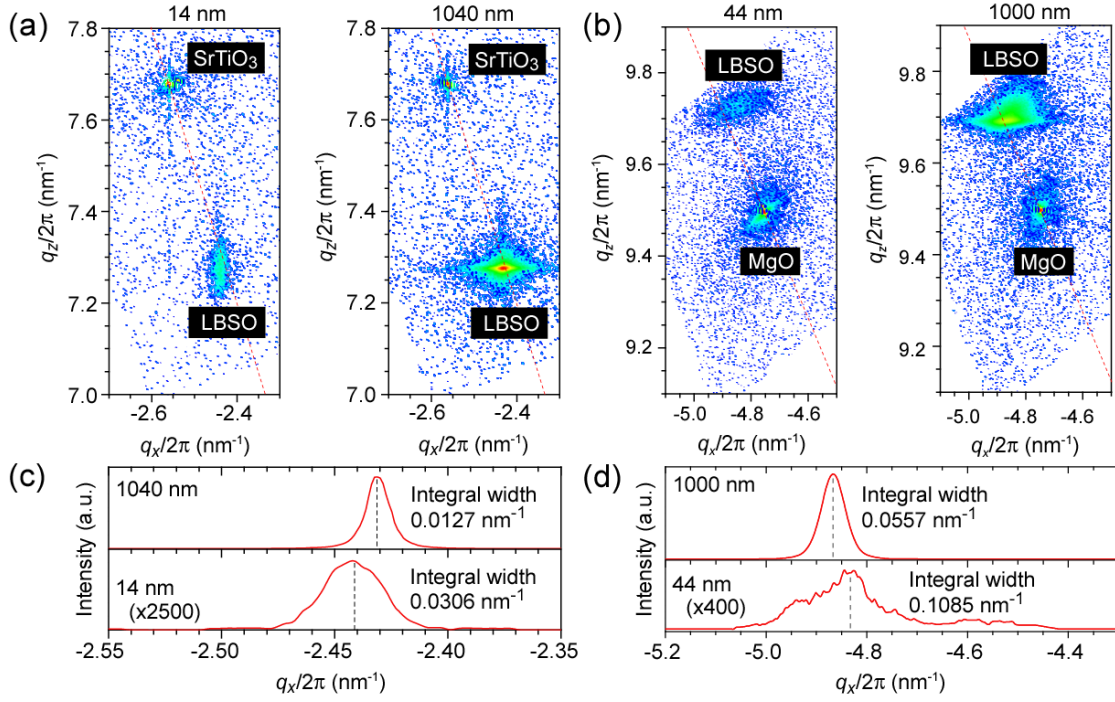
Figure 3.2 Crystallographic characterization of the LBSO epitaxial films grown on (001) SrTiO₃ and (001) MgO substrates. X-ray reciprocal space mapping around 103 LBSO on (a) (001) SrTiO₃ substrates (14-nm-thick and 1040-nm-thick films) and (b) (001) MgO substrates (44-nm-thick and 1000-nm-thick films). The red dotted lines show cubic symmetry. Cross-sectional intensity profiles of 103 LBSO peak on (c) (001) SrTiO₃ substrates (from (a)) and (d) (001) MgO substrates (from (b)).
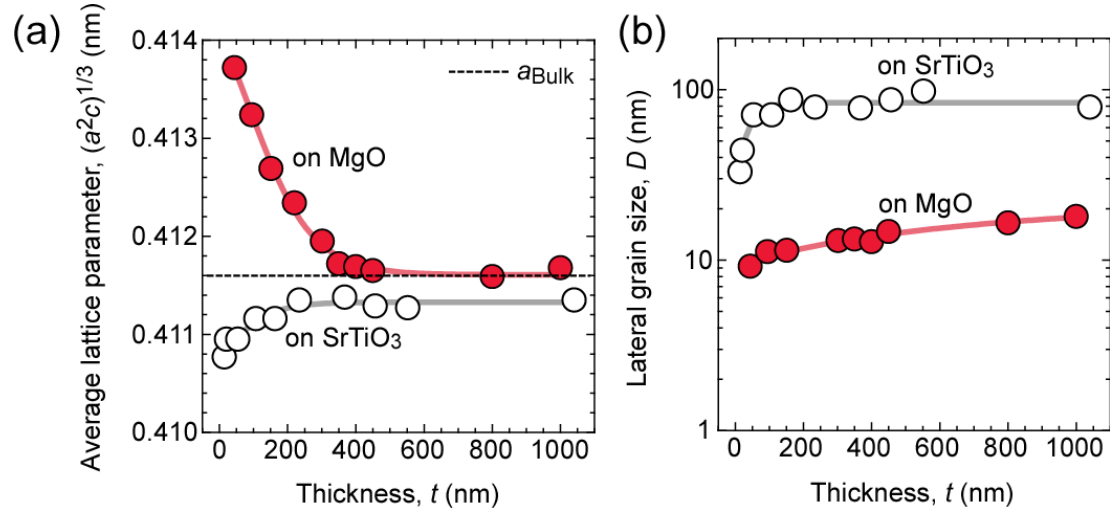
Figure 3.3 Thickness dependence of the crystal quality of the LBSO epitaxial films grown on (001) SrTiO₃ and (001) MgO substrates. (a) Average lattice parameters $(a^2c)^{1/3}$ and (b) lateral grain size (D) of the LBSO films grown on SrTiO₃ (white) and MgO (red).
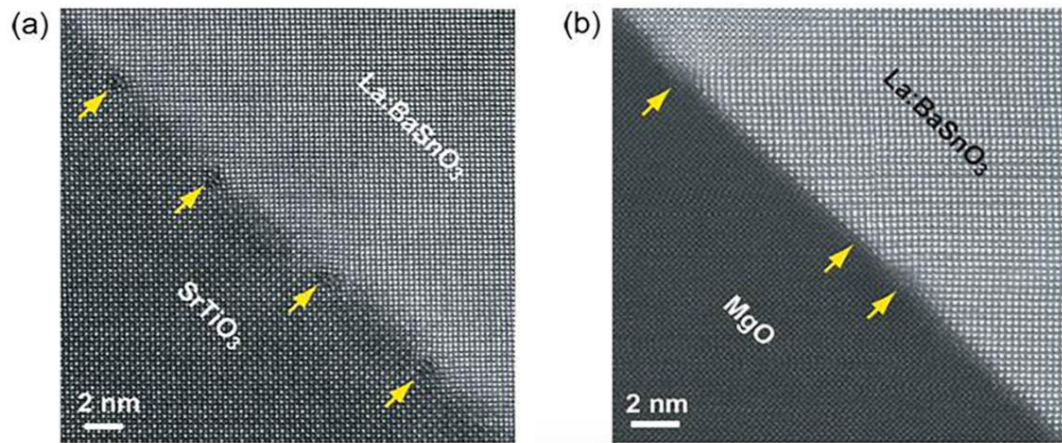
Figure 3.4 Cross-sectional HAADF-STEM images for the LBSO films grown on (a) (001) SrTiO₃ and (b) (001) MgO substrates. Periodically spaced dislocations are seen on SrTiO₃ substrates while dislocations on MgO substrates are randomly located.
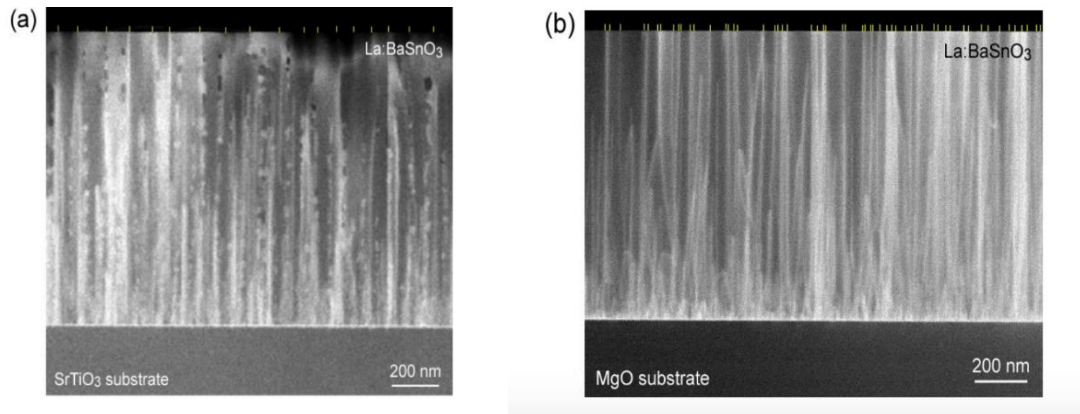
Figure 3.5 Cross-sectional LAADF-STEM images for the LBSO films grown on (a) (001) SrTiO$_3$ and (b) (001) MgO substrates. Threading dislocations are indicated with lines on the top surface of the LBSO films.
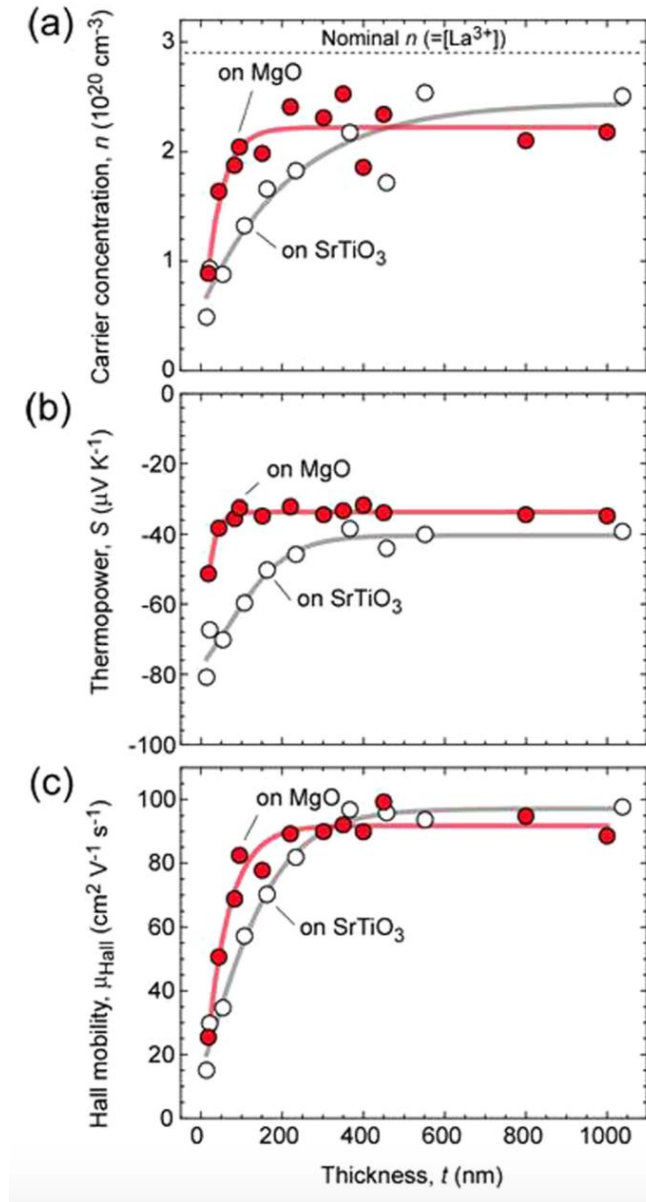
Figure 3.6 Thickness dependent electron transport properties of the LBSO films on SrTiO₃ and MgO substrates: (a) carrier concentrations, (b) thermopower, and (c) Hall mobility.
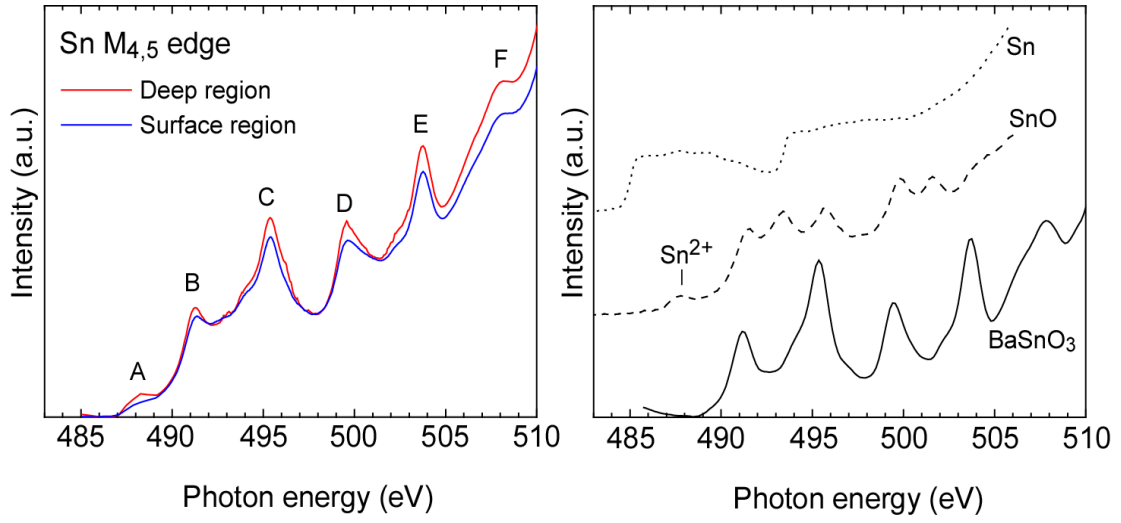
Figure 3.7 XAS around the Sn M$_{4,5}$ edge of a 500-nm-thick LBSO film on SrTiO$_3$ substrate. Additional Sn^{2+} can be observed in LBSO (left, A).
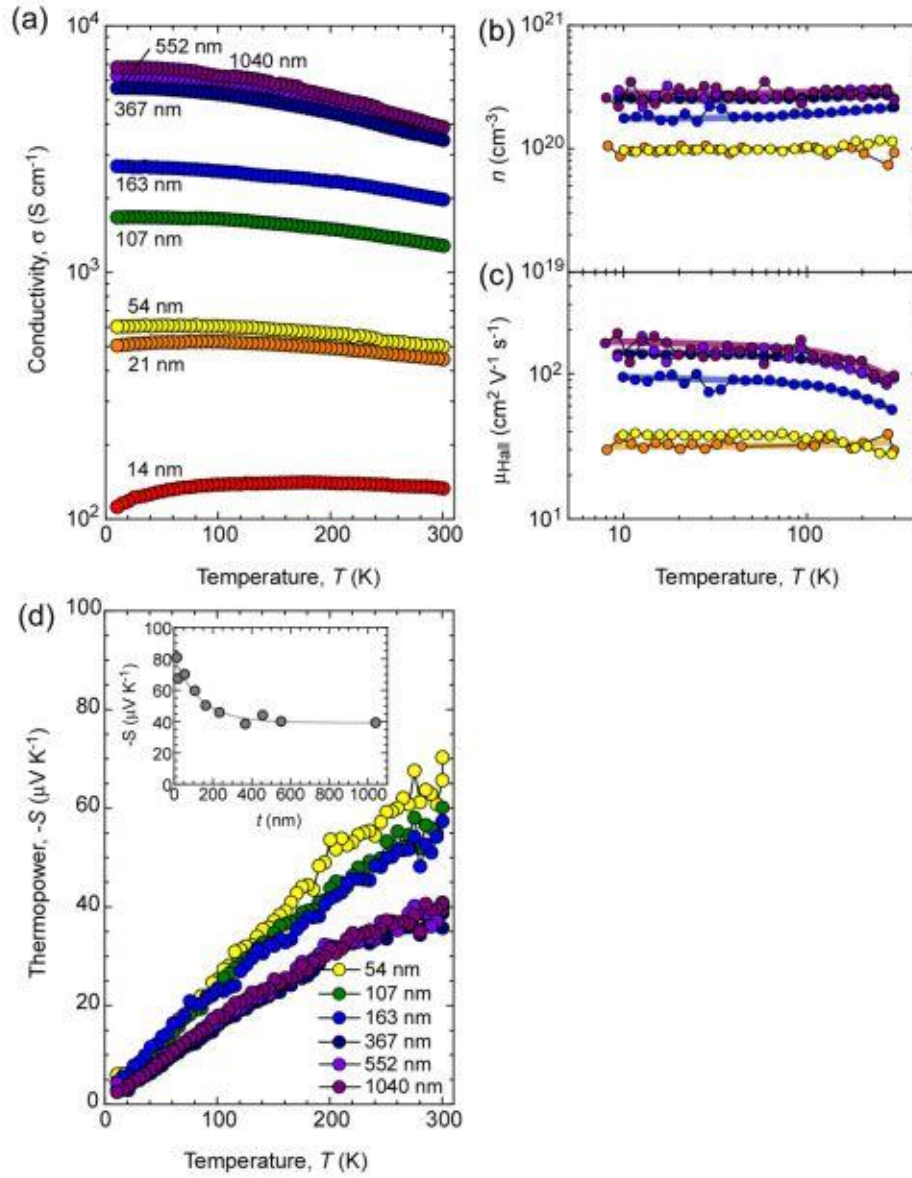
Figure 3.8 Temperature dependence of electron transport properties of LBSO epitaxial films grown on (001) SrTiO₃ substrate. (a) conductivity, (b) carrier concentration, (c) Hall mobility, (d) thermopower.

Chapter 4. Buffer Layer-Less Fabrication of High-Mobility Transparent Oxide Semiconductor, La-doped BaSnO₃

4.1 Objective of this chapter

Although the previous chapter showed that threading dislocations are not the main source of mobility suppression in LBSO films, many reports approach the mobility suppression and the charge carrier propagation hindrance from reducing threading dislocations or grain boundaries. Therefore, the most common method for enhancing the mobility of LBSO films is inserting thick undoped $BaSnO_3$ buffer layers between doped $BaSnO_3$ film and substrate to reduce the density of threading dislocations. For example, A. Prakash *et al.* optimized the thickness of buffer and LBSO layer and found that the ideal buffer layer thickness was 124 nm [67]; Shin *et al.* used buffer layer thickness of 150 nm whereas Shiogai *et al.* used 200 nm [60, 68]. Although these studies observed improved electron mobilities in LBSO films, the buffer layer insertion does not fully compensate the extra deposition step in the film fabrication process since the mobility values are still significantly low compared to that of bulk single crystals. This can be an issue for practical device applications because one-step fabrication processes are much more preferred in mass productions.

In the previous chapter, it was observed that the electron mobility of epitaxial LBSO films was strongly suppressed for films thinner than 50 nm. The mobilities increased with increasing thickness and eventually saturated at $90-100$ cm^2 V^{-1} s^{-1} (~200 nm on (001) MgO substrate and ~400 nm on (001) SrTiO₃ substrate). This implies that the initial several hundred nanometers in LBSO films play as buffer layers. Furthermore, the XAS spectrum of an LBSO film exhibited 2+ Sn valence states, which should not be detected from stoichiometric LBSO and suggest the presence of oxygen vacancies. Since the thickness dependence shows that the buffer region does not contribute much to the electron transport, the buffer region thickness needs to be reduced to achieve high mobility values without inserting additional buffer layers (**Figure 4.1**).

In this chapter, the results from the previous chapter was employed to design a one-step fabrication process for high-mobility LBSO films without inserting buffer layers. According to the existence of Sn^{2+} from the previous chapter, the driving hypothesis of this chapter regarded oxygen vacancies as the main lattice defects in the mobility suppressed buffer region (several hundred nanometers), which can be reduced by depositing the film under highly oxidative atmosphere (**Figure 4.1**). To reduce the formation of Sn^{2+} ions and oxygen vacancies in LBSO films [69], O₃ was injected during the film growth, which creates a much stronger oxidation environment compared to typically used O₂. The LBSO films grown in ozone (O₃-LBSO) indeed exhibited higher electron mobilities compared to the LBSO films deposited in oxygen (O₂-LBSO) without

inserting any buffer layer, especially for films thinner than 150 nm.

4.2 Experimental

2 %-La-doped LBSO epitaxial films were grown on (001) surface of $SrTiO_3$ substrates under O_3 and O_2 atmospheres using PLD technique. The substrate temperature was kept at 700 °C during the film growth, whereas the chamber pressures were 17 Pa for O_3-LBSO and 10 Pa for O_2-LBSO, respectively. In case of O_2-LBSO, only oxygen gas was injected in the chamber while the partial pressure of O_3 was set to 10% by an ozone generator for the synthesis of O_3-LBSO films. The films were annealed at 1200 °C in air to obtain the atomically smooth surfaces [56], and the thicknesses of the films varied from 11 nm to 450 nm.

4.3 Results and Discussion

All LBSO films were heteroepitaxially grown on the (001) $SrTiO_3$ substrates, which were confirmed by the XRD measurements. As shown in the **Figure 4.2**, stepped and terraced surfaces were observed in both O_3-LBSO and O_2-LBSO films. In order to clarify the structural differences in the LBSO films grown under O_3 and O_2 atmospheres in detail, the X-ray RSMs of the films were measured as shown in the **Figure 4.3**-**6**, respectively. In both cases, an asymmetric 103 diffraction spot of $BaSnO_3$ was observed around the 103 diffraction spot of $SrTiO_3$. Using these RSMs, both in-plane (*a-*) and cross-plane (*c-*)

lattice parameters were extracted as shown in **Figure 4.7 (a)**. Due to the large lattice

mismatch between LBSO and $SrTiO_3$ (−5 %), the lattice parameter a was much smaller

than the bulk value (0.4116 nm) whereas c was larger than the bulk value at the beginning

of the film growth (**Figure 4.7 (a)**). The a/(c) increased/(decreased) with increasing the

film thickness and approached the bulk value (0.4116 nm). It should be noted that the O_3-

LBSO showed larger differences from the bulk at the beginning of the film growth.

The average lattice parameter $(a^2 \cdot c)^{1/3}$ calculated from the RSMs is shown in **Figure 4.7**

(b), which represents the bulk strain in the films. Although the $(a^2 \cdot c)^{1/3}$ of the O_2-LBSO

films did not reach the bulk value, that of the O_3-LBSO increased drastically with the

thickness and almost reached the bulk value. These results suggest that the lattice

relaxation of the LBSO films occurred more quickly in the O_3 atmosphere. However, the

lateral grain size (D) of films from both atmosphere showed similar tendencies (**Figure**

4.7 (c)): at the beginning of the film growth, the D of the LBSO films were ~30 nm, which

increased with thickness and saturated when the thickness exceeded ~150 nm.

In order to further clarify the lattice strains, the microstructure of the films was observed

using LAADF-STEM as shown in **Figure 4.8**. While columnar structures were seen in

both the O_3-LBSO [**Figure 4.8 (a)**] and the O_2-LBSO films [**Figure 4.8 (b)**], the density

of the bright columns in the O_2-LBSO film is higher. Since the contrast in LAADF image

is sensitive to the strain field (*i.e.,* bulk strain), these results suggest that lattice strain was

be reduced under ozone atmosphere, which is in agrees with the RSM results.

The room temperture electron transport properties of the O_3-LBSO and O_2-LBSO films against the film thicknesses are summarized in **Figure 4.9**. The n in the LBSO films increased with the thickness and approached the nominal n_{nom}, which is defined by the atomic concentration of the La-dopants ($\equiv[2\%\text{-La}^{3+}] = 2.87 \times 10^{20}$ cm^{-3}). It should be noted that the n of O_3-LBSO films exhibited a much faster increase compared to O_2-LBSO films. For example, the n of ~100-nm-thick O_3-LBSO film is 87 % of the n_{nom} while that n of the O_2-LBSO film with the same thickness was only 46 % of the n_{nom} (**Figure 4.9 (a)**).

Similar trends were observed in the μ_{Hall} and σ of the LBSO films (*i.e.,* faster increase with thickness in O_3-LBSO); the μ_{Hall} of ~100-nm-thick O_3-LBSO film was 103 cm^2 V^{-1} s^{-1}, which is almost two times higher than 57 cm^2 V^{-1} s^{-1} for the O_2-LBSO film with the same thickness. The effect of the O_3 atmosphere can be clearly seen as O_3-LBSO films always exhibited significantly higher μ_{Hall} values compared to O_2-LBSO films at the same thickness (**Figure 4.9 (b) and (c)**). The highest μ_{Hall} value (115 cm^2 V^{-1} s^{-1}) was observed in the 452-nm-thick O_3-LBSO film. In addition, the thermopower ($-S$) of the LBSO films decreased with increasing thickness (**Figure 4.9 (d)**), and the S declination rate of O_3-LBSO films was much higher than that of O_2-LBSO films (**Figure 4.9 (d)**). Since $|S|$ decreases with n [70], the observed $-S$ reduction is consistent with the thickness

dependence of *n* (**Figure 4.9 (a)**). These results show that LBSO films grown under O₃ atmosphere exhibit improved electron transport properties.

To validate the initial hypothesis on the role of oxygen deficiencies on the formation of Sn^{2+} states [69], XAS was performed around the Sn $M_{4,5}$ edge of ~100-nm-thick LBSO films on SrTiO₃ substrate. Surface sensitive electron yield mode was used (the penetration depth of X-ray ~10 nm). The XAS spectra of the LBSO films are shown in **Figure 4.10**. In both films, four absorption peaks from stoichiometric Sn^{4+} ions were observed (**Figure 4.10 (a)**), which agree with other studies [39, 71, 72]. Interestingly, just as intended, Sn^{2+} peak at ~488 eV disappeared in the O₃-LBSO film and can only be seen from the XAS of O₂-LBSO film (**Figure 4.10 (a)**) [71, 73, 74]. The thicknesses of the O₂-LBSO and O₃-LBSO films were 107 nm and 125 nm, respectively. Despite the similar thickness values, the μ_{Hall} of the O₂-LBSO film (57 cm² V⁻¹ s⁻¹) was much lower compared to that of the O₃-LBSO film (103 cm² V⁻¹ s⁻¹). This result suggests that the existence of the Sn^{2+} ion can indeed be related to the mobility suppression of LBSO films.

In the stoichiometric composition of BaSnO₃, the stable valence state of Sn is 4+. If the two extra electrons from an oxygen vacancy form Sn^{2+} ion, the Sn^{2+} ions may degrade the carrier generation efficiency of La^{3+} ions and scatter electrons. Therefore, it is plausible for oxygen deficiencies to reduce the transport properties of electrons in LBSO.

In fact, MBE-grown LBSO films with high mobility were fabricated using highly oxidative atmosphere [37, 38, 67]. Thus, in the context of this chapter, it can be suspected that low mobility and low carrier concentration in LBSO films observed in other studies are related to the non-oxidative atmosphere. The mobility dependence on the thickness suggest that these defects are concentrated at the film/substrate interface. However, it should be noted that the formation of Sn^{2+} states and oxygen vacancies in LBSO needs to be studied much more thoroughly to clarify their exact location in the film.

4.4 Conclusions

In this chapter, the electron mobility of LBSO films was successfully improved without inerting buffer layers by using highly oxidative atmosphere (O_3) during the film growth. The lattice relaxation of the O_3-LBSO films occurred when the film thickness was thinner than the O_2-LBSO films. Despite being smaller than single crystal values, the highest electron mobility observed here (115 cm^2 V^{-1} s^{-1}) is among the highest in LBSO films on SrTiO$_3$ substrates and similar to LBSO films with buffer layers. The XAS results showed that the Sn^{2+} concentration in the LBSO films was successfully reduced by creating an oxidative atmosphere during the film growth with the injection of O_3.
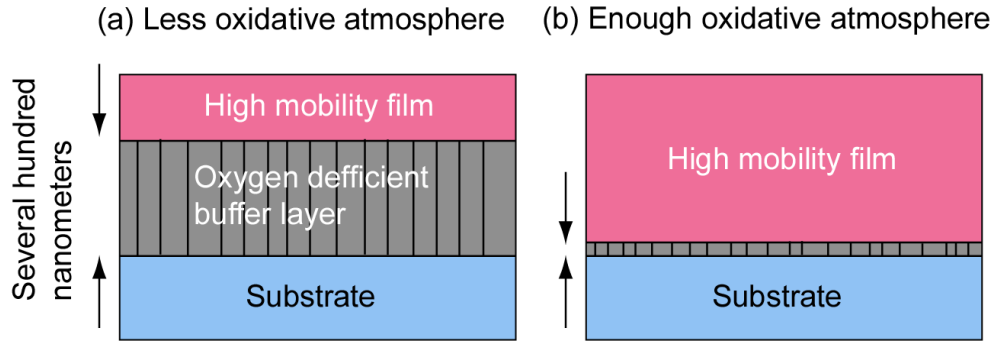
Figure 4.1 Hypothesis: Schematic illustration of LBSO films. (a) LBSO film grown under less oxidative atmosphere. Since the buffer layer is not fully oxidized, several hundred nanometer thick oxygen deficient buffer layer is initially grown on the substrate. After the lattice relaxation, high mobility LBSO film growth occurs. (b) LBSO film grown under enough oxidative atmosphere. A fully oxidized buffer layer is initially formed on the substrate. The lattice relaxation occurs in the thinner film, after that, high mobility LBSO film growth occurs. It is suspected that the buffer layer thickness should be very high to achieve the high mobility for low oxidative atmosphere since the buffer contains oxygen deficiency. On the other hand, buffer layer thickness highly reduced by using enough oxidative atmosphere to acquiring high mobility, which will be useful for practical application.
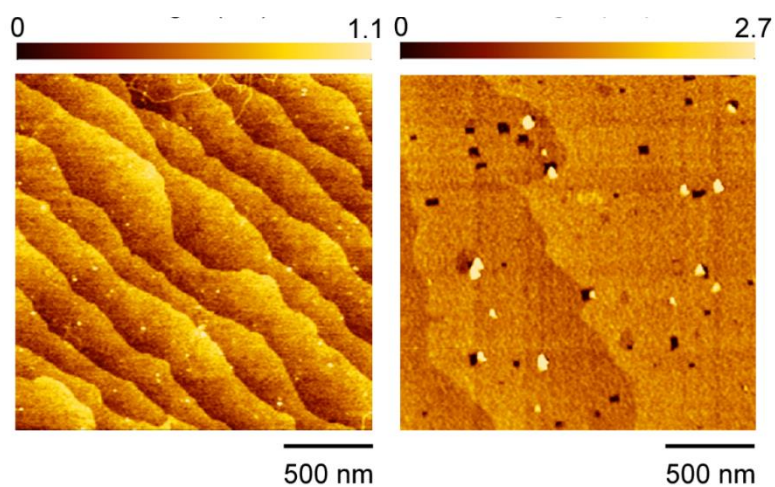
Figure 4.2 Topographic AFM images of the LBSO films grown on (001) SrTiO₃
under oxygen (left) and ozone (right) atmosphere.
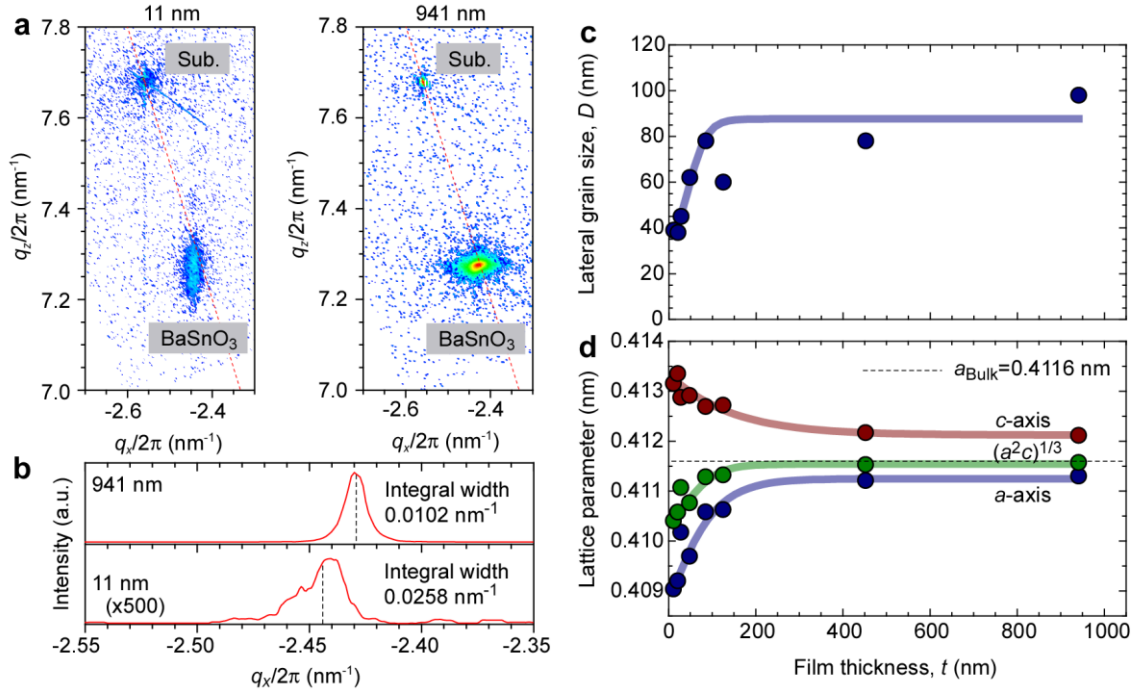
Figure 4.3 Crystallographic characterizations of the O₃-LBSO films grown on (001) SrTiO₃ substrates. (a) RSMs of asymmetric (103) diffraction of O₃-LBSO films. The symmetry axis of a cubic lattice is indicated by a red line. (103) BaSnO₃ diffraction peak approaches the red line, which suggests that lattice strain due to the film/substrate mismatch is gradually deceasing; (b) the cross-sectional intensity plot along the in-plane axis in reciprocal space ($q_x/2\pi$); (c) thickness dependence of the lateral grain sizes; (d) thickness dependent lattice parameter along the in-plane direction (blue), out-of-plane direction (red), and the average lattice parameter (green). All these values approach the lattice parameter of bulk LBSO (black dashed line) with increasing film thickness.

Figure 4.4 RSMs of O₃-LBSO films grown on (001) SrTiO₃ substrate around the (103) Bragg diffraction. The thicknesses of the films were (a) 11 nm, (b) 21 nm, (c) 28 nm, (d) 48 nm, (e) 85 nm, (f) 125 nm and (g) 452 nm.
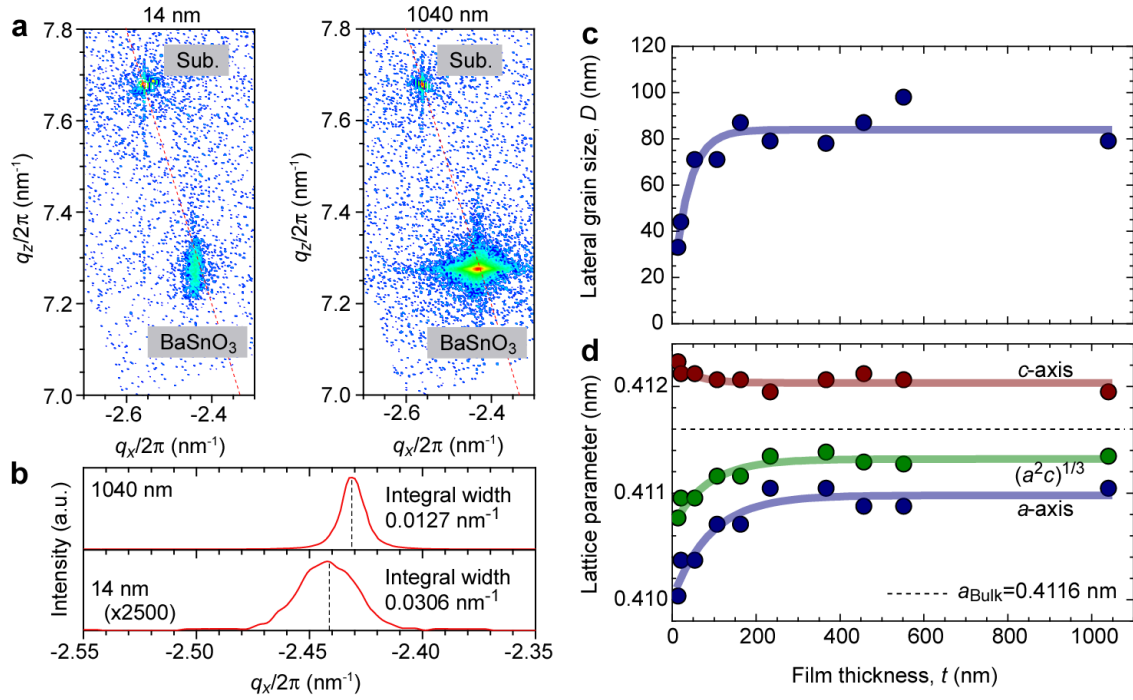
Figure 4.5 Crystallographic characterizations of the O₂-LBSO films grown on (001) SrTiO₃ substrates. (a) RSMs of asymmetric (103) reflection of O₃-LBSO films. The symmetry axis of a cubic lattice is indicated by a red line. (103) BaSnO₃ diffraction peak approaches the red line, which suggests that lattice strain due to the film/substrate mismatch is gradually deceasing; (b) the cross-sectional intensity plot along the in-plane axis in reciprocal space ($q_x/2\pi$); (c) thickness dependence of the lateral grain sizes; (d) thickness dependent lattice parameter along the in-plane direction (blue), out-of-plane direction (red), and the average lattice parameter (green). All these values approach the lattice parameter of bulk LBSO (black dashed line) with increasing film thickness. The crystallographic characteristics of O₂-LBSO films were very similar with those of O₃-LBSO films.
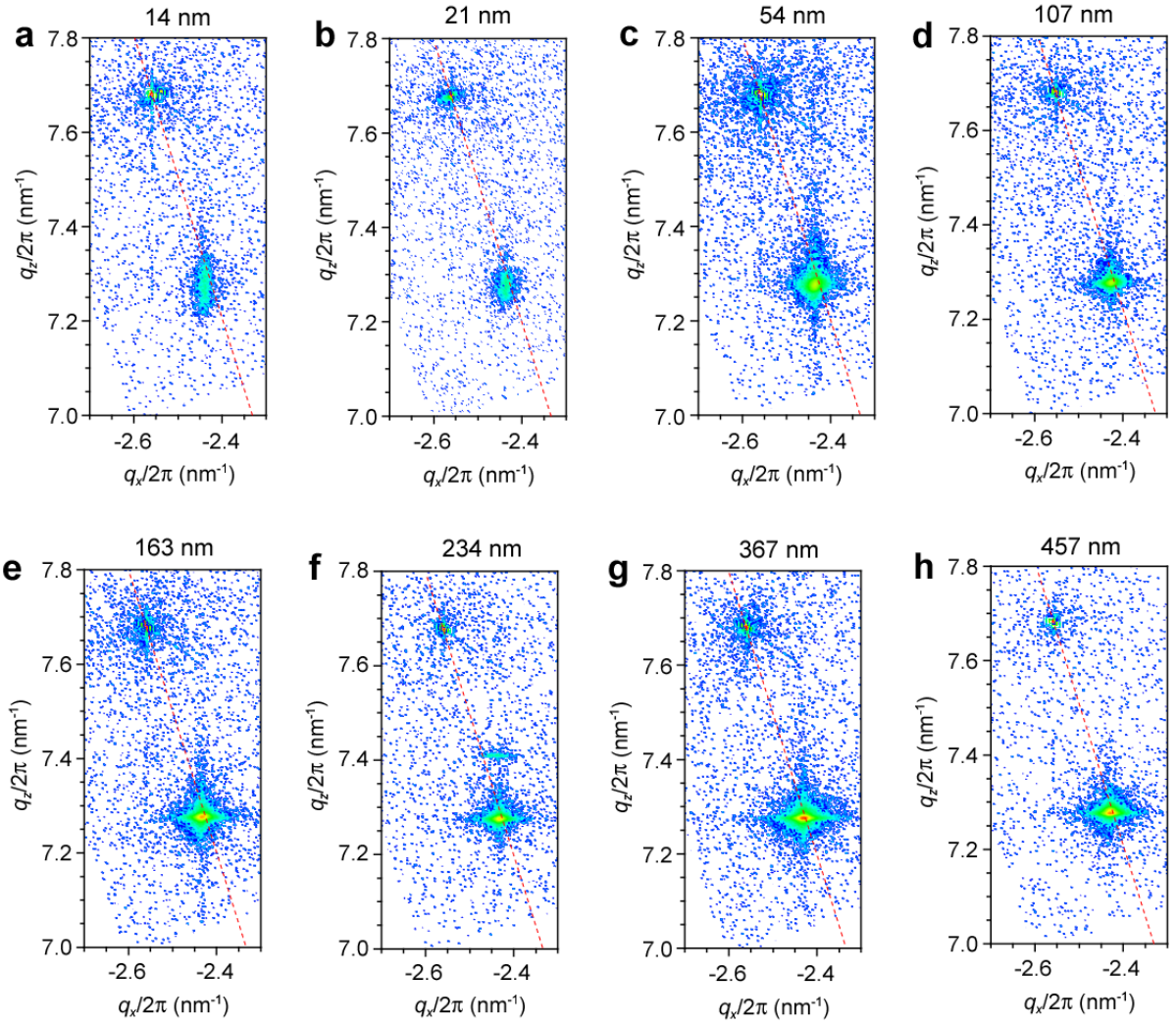
Figure 4.6 RSMs of O₂-LBSO films grown on (001) SrTiO₃ substrates around the (103) Bragg diffraction. The thicknesses of the films were (a) 14 nm, (b) 21 nm, (c) 54 nm, (d) 107 nm, (e) 163 nm, (f) 234 nm, (g) 367 nm, and (h) 457 nm.
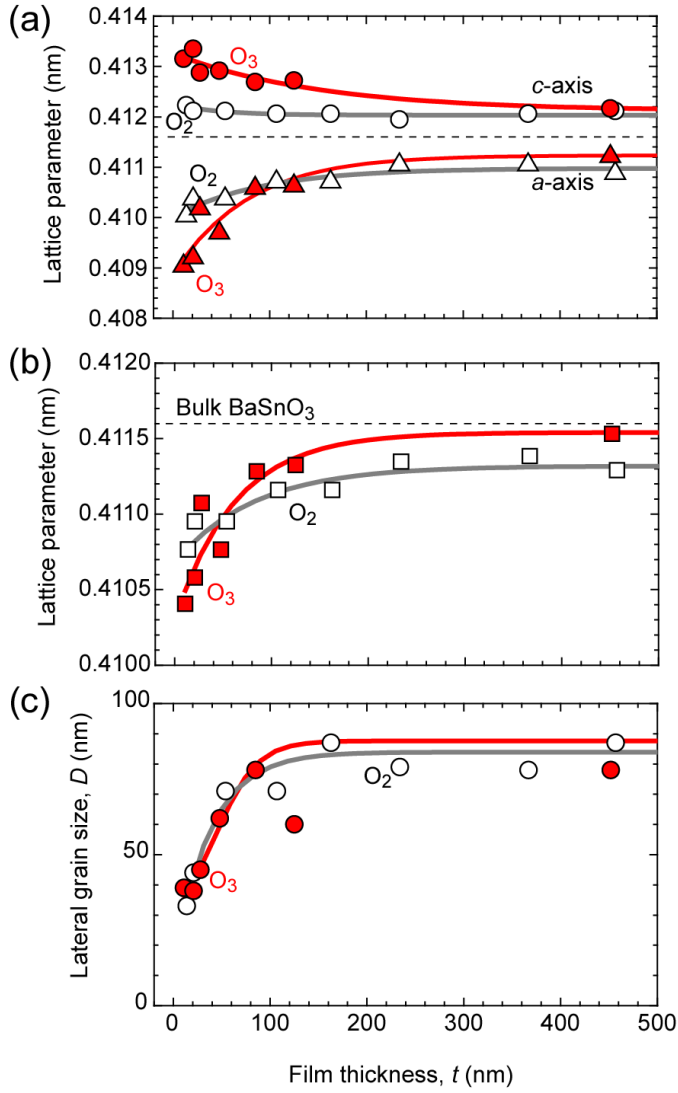
Figure 4.7 Lattice characteristics of the LBSO films at room temperature. Thickness dependences of (a) lattice parameters, *a* and *c*, (b) average lattice parameter $(a^2 \cdot c)^{1/3}$, and lateral grain size for the resultant LBSO films grown under ozone (filled symbols) and oxygen (open symbols) atmospheres. Average lattice parameter of the O_3-LBSO increased dramatically with the thickness and almost reached the bulk value (0.4116 nm).
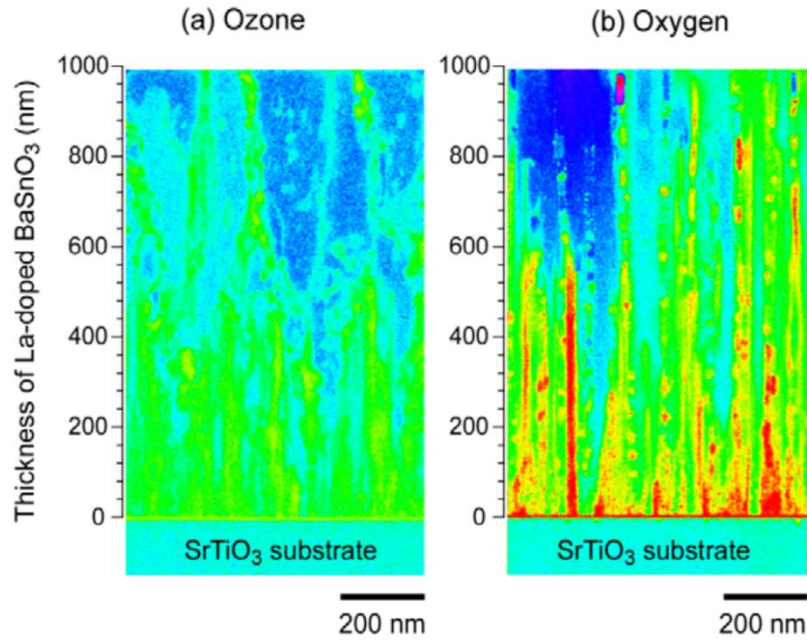
Figure 4.8 Cross-sectional LAADF-STEM images of the LBSO films. Columnar structure is seen in both (a) the O₃-LBSO and (b) the O₂-LBSO films. The strain contrast in O₃-LBSO is lower.
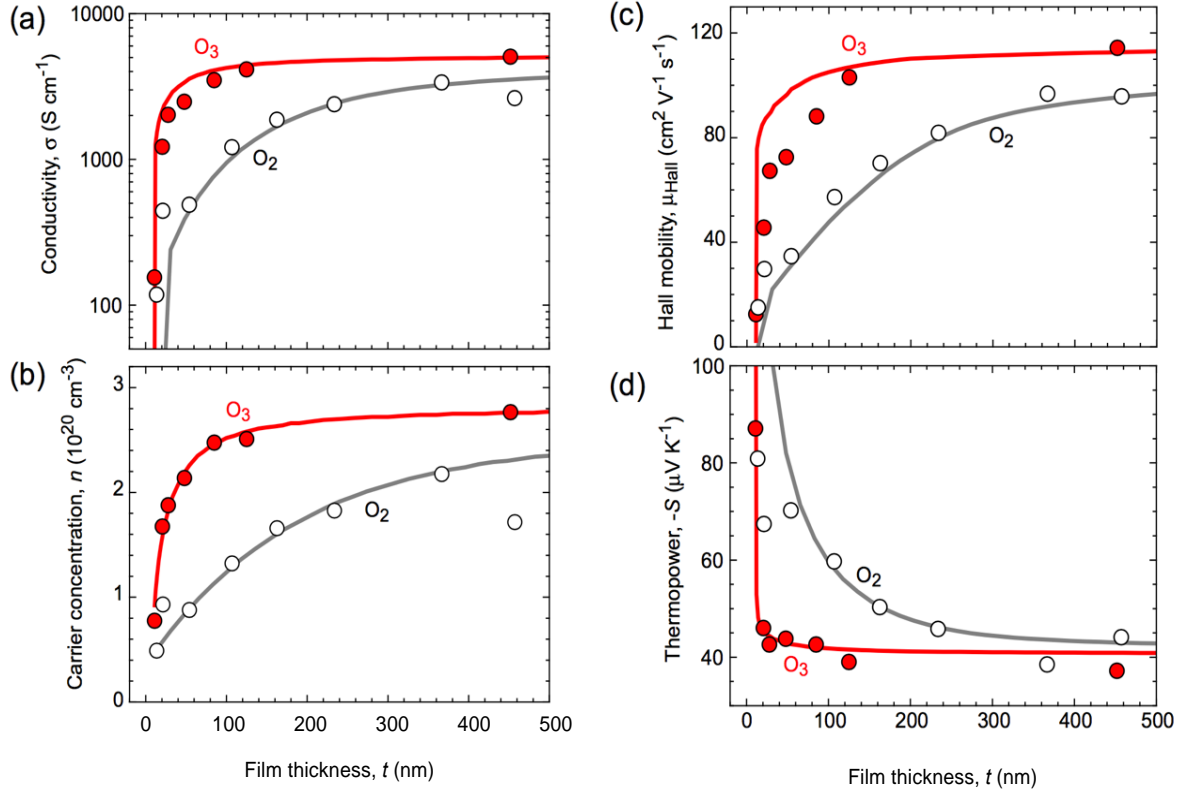
Figure 4.9 Electron transport properties of the LBSO films. The O₃-LBSO (red) and the O₂-LBSO films: (a) conductivity, (b) carrier concentration, (c) Hall mobility, and (d) thermopower.
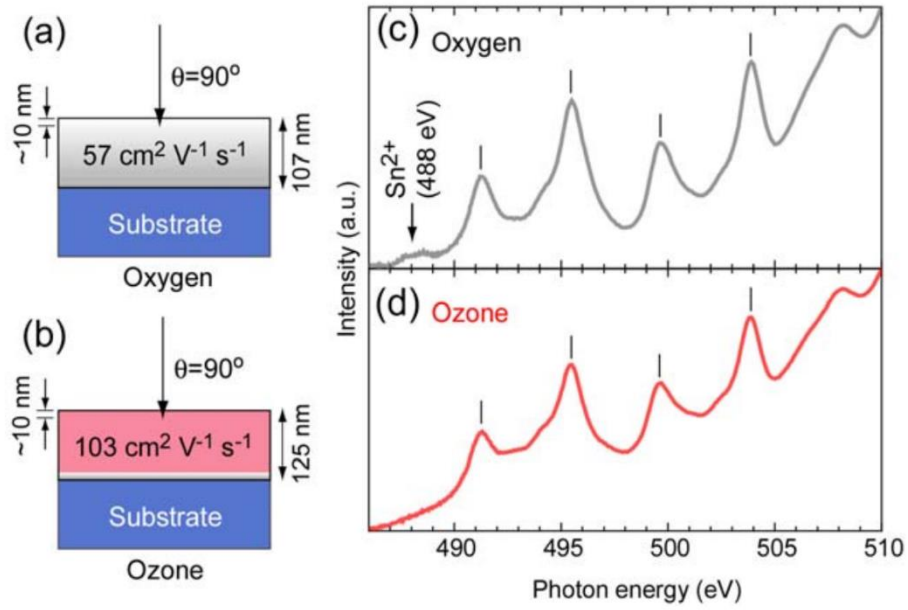
Figure 4.10 XAS spectra of the LBSO films. (a, b) Schematic cross-sectional structure and (c, d) XAS spectra at around the Sn $M_{4,5}$ edge of the LBSO films. Sn^{2+} peak is not observed in the O_3-LBSO film.

Chapter 5. High Electrical Conducting Deep-Ultraviolet-Transparent Oxide Semiconductor, La-doped SrSnO₃

5.1 Objective of this chapter

Despite the excellent electron transport properties, applications of LBSO is limited to visible range, and optoelectronic engineers search for transparency in other ranges too. DUV (200−300 nm in wavelength)TOSs have attracted attention as transparent electrodes for DUV optoelectronic devices such as DUV light emitting diode and DUV detector for biological applications because most DNA show their absorption peaking around 260 nm in wavelength [75]. Among several DUV-TOSs, LSSO (E_g ~4.6 eV) is one of the most promising materials since LSSO can be grown heteroepitaxially on the single crystalline substrates such as MgO [76], SrTiO₃ [77], and KTaO₃ [78]. Further, the electrical conductivity of LSSO films (~1000 S cm^{-1}) [45] is larger than other well-known DUV-TOSs such as β-Ga₂O₃ (~1 S cm^{-1}) [20, 21], α-Ga₂O₃ (~0.3 S cm^{-1}) [22], electron-doped calcium aluminate (C12A7, ~800 S cm^{-1}) [23-25], and recently developed Al:Mg$_{0.43}$Zn$_{0.57}$O (~400 S cm^{-1}) [35]. However, the electrical conductivity of LSSO films is still much lower than that of commercially available transparent conducting oxide ITO.

The crystal structure of SrSnO₃ is regarded as pseudo-double-cubic perovskite (*a* =

0.8068 nm) [79] although the real lattice is orthorhombic [80]. Several researchers fabricated the epitaxial films of LSSO by using vapor phase epitaxy method such as PLD and MBE. However, due to difficulties in growing high-quality conductive LSSO films, their electron transport properties have not been extensively studied compared to the optical properties and electronic structures. Baba *et al*. reported that the electrical conductivity of 5% La-doped LSSO film on lattice matched $NdScO_3$ substrate was ~1000 S cm^{-1} [45], which is the highest electrical conductivity to date. However, the carrier concentration was only 2.5×10^{20} cm^{-3}, which was only ~1/3 of La concentration, [La]. To improve the electrical conductivity of LSSO films, the activation of La dopants in the LSSO lattice needs to be enhanced.

In this chapter, in order to enhance the activation of La dopants, the LSSO films were annealed at 790 °C in vacuum (<10^{-2} Pa). In case of LBSO films, annealing in oxygen reducing atmospheres enhance the lateral grain size. Therefore, it can be suspected that the point defect formation during the annealing in vacuum would induce grain growth and increase the activation of La dopants in LSSO films. After annealing, grain growth was indeed observed in LSSO films from ~10 nm to ~28 nm, and the electron transport properties of the annealed LSSO films were significantly improved. This chapter reports highly conducting (>3000 S cm^{-1}) LSSO thin films fabricated by PLD on MgO (E_g ~7.8 eV) [81] substrate followed by a simple annealing in vacuum.

5.2 Experimental

La$_x$Sr$_{1-x}$SnO$_3$ (x = 0.005, 0.02, 0.03 and 0.05) epitaxial films were fabricated on (001) MgO (a = 0.4212 nm) single crystal substrates using PLD technique. During the film growth, substrate temperature and oxygen pressure inside the chamber were kept at 790 °C and 20 Pa, respectively. Conducting LSSO film was not obtained when the oxygen pressure was lower than 20 Pa, indicating that oxygen vacancies do not play as the electron donor, similar to LBSO. After the film growth, the substrate heater was immediately turned off, and the sample was cooled down to room temperature. The resultant film was annealed in vacuum at 790 °C for 30 mins.

5.3 Results and Discussion

The lateral grain sizes can be observed from the RSM of the resultant LSSO film (x = 0.03, as grown) measured around 204 diffraction spot of LSSO (**Figure 5.1 (a)**). Broad diffraction spot of 204 LSSO is seen peaking at ($q_x/2\pi$, $q_z/2\pi$) = (−4.97 nm^{-1}, 9.88 nm^{-1}) together with the 204 diffraction spot of MgO at (−4.75 nm^{-1}, 9.50 nm^{-1}), indicating that incoherent epitaxial growth occuured. The lateral grain size was ~12 nm, which was calculated by Scherrer's equation and the cross sectional diffraction pattern along $q_x/2\pi$ direction.

In order to increase the lateral grain size, the LSSO films were annealed at 790 °C in

vacuum ($<10^{-2}$ Pa) for 30 min and cooled down to room temperature. After the vacuum

annealing, the 204 diffraction spot intensity increased as shown in **Figure 5.1 (b)**, and the

lateral grain size was successfully increased up to 28 nm. Similar increase in the

diffraction spot intensity was observed in all cases ($x = 0.005, 0.02$ and 0.05) as shown in

Figure 5.6. Using the 204 diffraction spots, the average lattice parameters, $(a^2 \cdot c)^{1/3}$ of the

LSSO films were determined before and after annealing (**Figure 5.1 (c)**). The annealed

films showed more relaxation, which is likely attributed to the grain growth. Note that

this annealing condition is the optimized condiciton among air, 1 Pa oxygen, and vacuum

($<10^{-2}$ Pa). Significant grain growth was observed when the LSSO film was annealed in

vacuum. This is consistent with the observation of accelerated dislocation movement due

to oxygen vacancy-assisted recovery in ionic crystals [82]. According to previous studies

on stannate films, extra charge carriers from oxygen vacancies are compensated by the

formation of charge accepting *A*-site vacancies [83]. Therefore, any carrier concentration

changes that may result from the vacuum annealing are likely attributed to the activation

of La dopants. In addition, no conducting LSSO film was obtained when undoped SrSnO₃

film was annealed in vacuum, which means that oxygen vacancy does not significantly

affect carrier generation.

In order to further confirm the grain growth due to the vacuum annealing, the

microstructures of the LSSO films were observed using LAADF-STEM. While columnar

structures were observed for both the as-deposited (**Figure 5.2 (a)**) and annealed LSSO

films (**Figure 5.2 (b)**), the width of the columns for the annealed LSSO film was significantly greater. This indicates that the vacuum annealing indeed induces grain growth, which is in excellent agreement with the RSM results. It should be noted that incoherent interfaces with misfit dislocations was observed at the interface between the LSSO film and MgO substrate in both cases as shown in **Figure 5.2 (c)** and **Figure 5.2 (d)**, indicating that the interface structures were not affected by the vacuum annealing.

Figure 5.3 summarizes the electron transport properties of the resultant LSSO films at room temperature. Both carrier concentration and Hall mobility gradually increased with [La] until [La] = 3% and decreased at [La] = 5%, probably due to the low solubility limit of La in $SrSnO_3$ lattice, which is similar to LBSO. Significant enhancements in the electron transport properties were observed in the vacuum annealed LSSO films. Compared to the as grown LSSO films, the annealed LSSO films showed greater σ (**Figure 5.3 (a)**), n (**Figure 5.3 (b)**), and μ_{Hall} (**Figure 5.3 (d)**) at room temperature while the largest enhancement was observed in 5% La doped LSSO film. The absolute value of S for LSSO films decreased after annealing (**Figure 5.3 (c)**). This is consistent with the fact that carrier concentration increased after annealing. The activation rate of La ion (**Figure 5.3 (e)**), which was calculated as $n \cdot [La]^{-1}$ assuming La^{3+} ions solely generate carrier electrons, increased after the vacuum annealing. Thus, the increased σ and μ_{Hall} of annealed films are probably attributed to the improved efficiency of the carrier activation from the La dopant and the grain growth. In other words, carrier electrons are more

efficiently provided in the annealed films. The highest σ and μ_{Hall} were observed from

annealed 3%-La doped LSSO films, of which the activation of La ion and lateral grain

size showed the largest value.

The experimental m^* value of the LSSO epitaxial films was also clarified by the

relationship of S and n of resultant films at room temperature (**Figure 5.4 (a)**). Since n

and S values both are only sensitive to the density of states and Fermi level, the m^* was

calculated using the following equations [84].

$$S = -\frac{k_B}{e}\left(\frac{(r+2)F_{r+1}(\xi)}{(r+1)F_r(\xi)} - \xi\right)$$

(1)

where k_B, ξ, r, and F_r are the Boltzmann constant, reduced Fermi energy, scattering

parameter of relaxation time, and Fermi integral, respectively. The r value was assumed

to be 0.5 (acoustic phonon scattering) because the temperature dependence of Hall

mobility showed that phonon scattering is dominant at room temperature. F_r and n are

given by,

$$F_r(\xi) = \int_0^\infty \frac{x^r}{1+e^{x-\xi}}\,dx$$

(2)

$$n_- = 4\pi\left(\frac{2m^*k_BT}{h^2}\right)^{3/2} F_{1/2}(\xi)$$

(3)

where h and T are the Planck constant and absolute temperature, respectively. Most of the

$S - n$ plots ($n > 10^{20}$ cm^{-3}) are located on the line obtained from $m^* = 0.23\ m_0$, similar to

that of Ba$_{0.5}$Sr$_{0.5}$SnO$_3$, though two points ($n < 10^{20}$ cm^{-3}) are located on the lower side,

probably due to the contribution of the tail state around the CBM.

Figure 5.4 (b) summarizes the μ_{Hall} of the LSSO epitaxial films as a function of n at room temperature. The values reported by Wang *et al*. and Baba *et al*. are also plotted for comparison [85, 45]. The μ_{Hall} increased with increasing n. The highest μ_{Hall} and electrical conductivity were observed from 3% La-doped LSSO film. The μ_{Hall} reached 55.8 cm^2 V^{-1} s^{-1} at a n of 3.26×10^{20} cm^{-3}, which a record high value reported from LSSO films. Moreover, an electrical conductivity exceeding 3000 S cm^{-1} was achieved in the annealed 3% La-doped LSSO film, which is much higher than that of many other DUV transparent conducting oxides.

Finally, the optical transmission and reflection spectra of the vacuum annealed 3% La-doped LSSO film (thickness: 112 nm) grown on double side polished (001) MgO substrate are shown in the inset of **Figure 5.5**. The optical transmission in the deep UV region was kept ~70 % at 300 nm and exceeded 25 % at 260 nm, which is the absorption peak wavelength of most DNAs. Although SrSnO₃ has an indirect bandgap [86], the bandgap was estimated by assuming a direct bandgap for simplicity; $(\alpha{\cdot}h{\cdot}v)^2$−photon energy plot was used to estimate the bandgap of the LSSO film (**Figure 5.5**), where α is the absorption coefficient and v is speed of light. The bandgap obtained was ~4.6 eV, agreeing well with the reported values. The α at 260 nm in wavelength was calculated to be 8.3×10^4 cm^{-1}; the penetration depth of 260 nm light in LSSO is ~120 nm, which is

the origin of low transmission (25%) in the 260 nm light through the 112 nm LSSO film. Thus, most of the 260 nm light can transmit through LSSO film when the thickness is thinner. From these results, it can be concluded that present LSSO film, which exhibited high electrical conductivty of ~3000 S cm^{-1} and deep UV transparency, would be useful as the transparent electrode for developing DUV-transparent optoelectronic devices for biological applications. The figure-of-merit φ_{TC} (= T^{10}/R_s, T is transmission and R_s is the sheet resistance) [87] of the present LSSO film is 14.5×10^{-3} Ω^{-1}, which is four orders magnitude higher than that of β-Ga$_2$O$_3$ ($\varphi_{TC} = 7.8 \times 10^{-7}$ Ω^{-1}) at 300 nm.

5.4 Conclusions

In this chapter, highly conducting (>3000 S cm^{-1}) LSSO thin films with an optical bandgap of ~4.6 eV were fabricated. From the XRD and the STEM analyses, it was found that lateral grain growth occurred during the vacuum annealing, which improved the activation rate of La ion, leading to significant improvements in the carrier concentration (3.26×10^{20} cm^{-3}) and Hall mobility (55.8 cm^2 V^{-1} s^{-1}). The optical transmission at 300 nm was ~70 % and that at 260 nm exceeded 25 %. The present DUV-TOS would be useful as the transparent electrode in DUV-transparent optoelectronic devices, especially for biological applications.
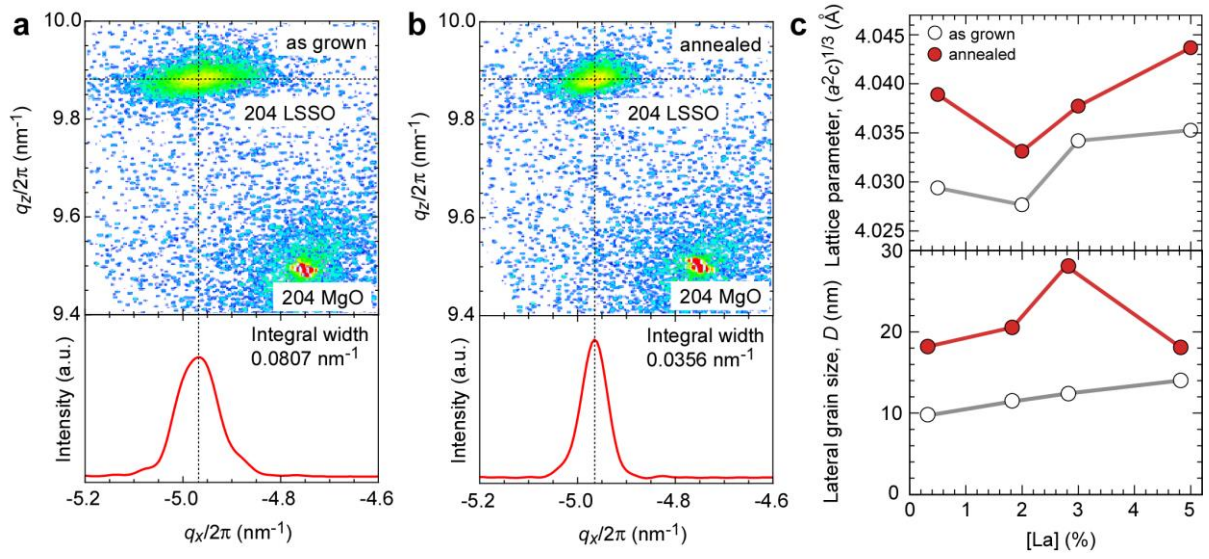
Figure 5.1 Lateral grain growth of the LSSO films by vacuum annealing. (a, b) RSMs around 204 LSSO diffraction spot of (a) as grown and (b) annealed films. The cross-sectional diffraction patterns along $q_x/2\pi$ direction are shown at the bottom of each RSM. (c) Changes in (upper) the average lattice parameter and (lower) lateral grain size of the as-deposited LSSO films (white) and annealed LSSO films (red) as a function of La concentration in the target materials. The vacuum annealing substantially increased the lateral grain size.
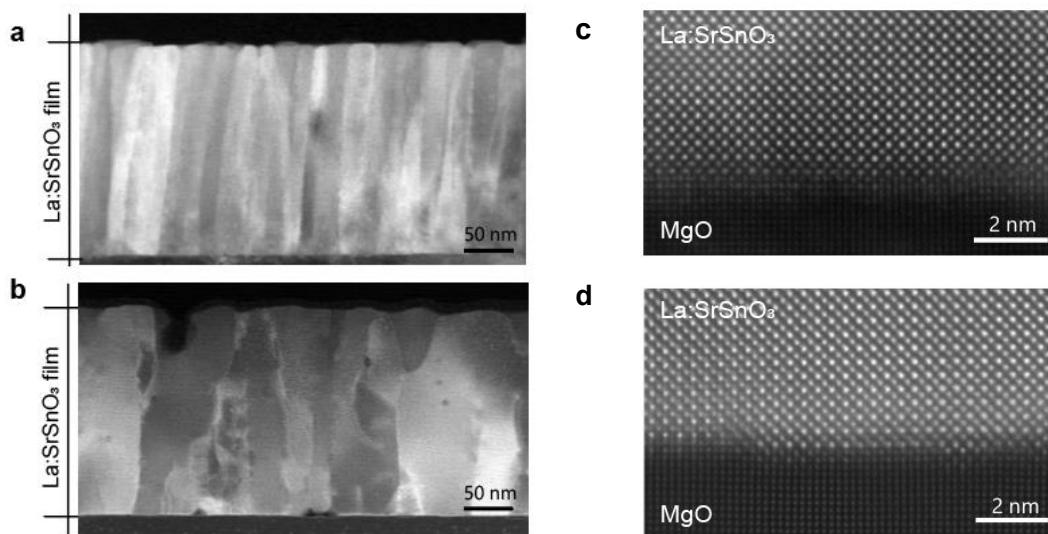
Figure 5.2 Cross-sectional LAADF-STEM images for the LSSO films. (a, c) as grown and (b, d) annealed LSSO films. The lateral grain growth of annealed LSSO films is clearly visualized. Incoherent interfaces with misfit dislocations are seen at the interface between the LSSO film and MgO substrate in both cases. The interfaces are not affected by the vacuum annealing.
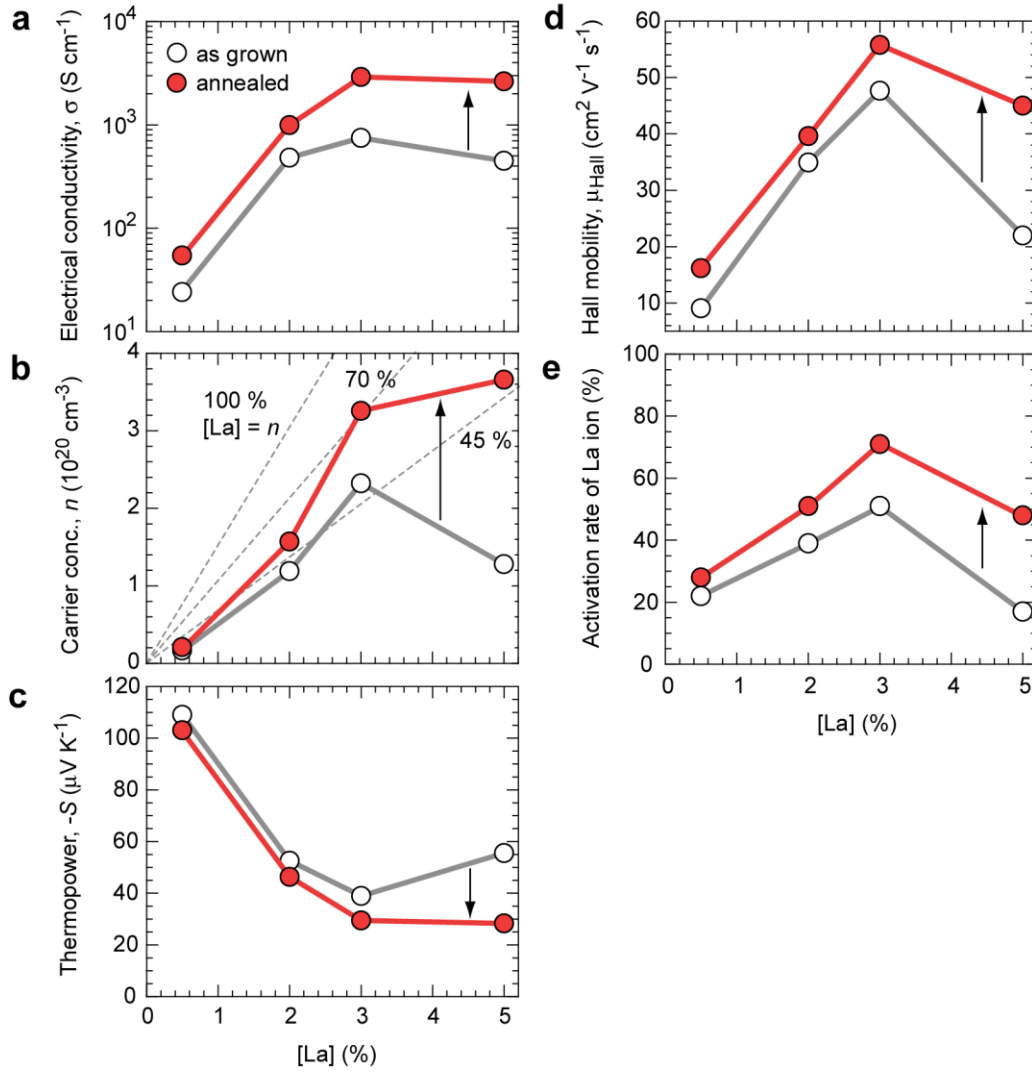
Figure 5.3 Electron transport properties of the resultant LSSO thin films as a function of La content (%) at room temperature. (a) Electrical conductivity (σ), enhancement of σ for the vacuum annealed LSSO films increased with the La content. (b) Carrier concentration (n). n of LSSO film increased after annealing in vacuum. (c) Thermopower ($-S$). The absolute value of thermopower (S) decreased after annealing. (d) Hall mobility (μ_{Hall}). The μ_{Hall} of the annealed LSSO films was largely enhanced at 5% La^{3+}. (e) Activation rate of La ion. After vacuum annealing, La ion became more active.
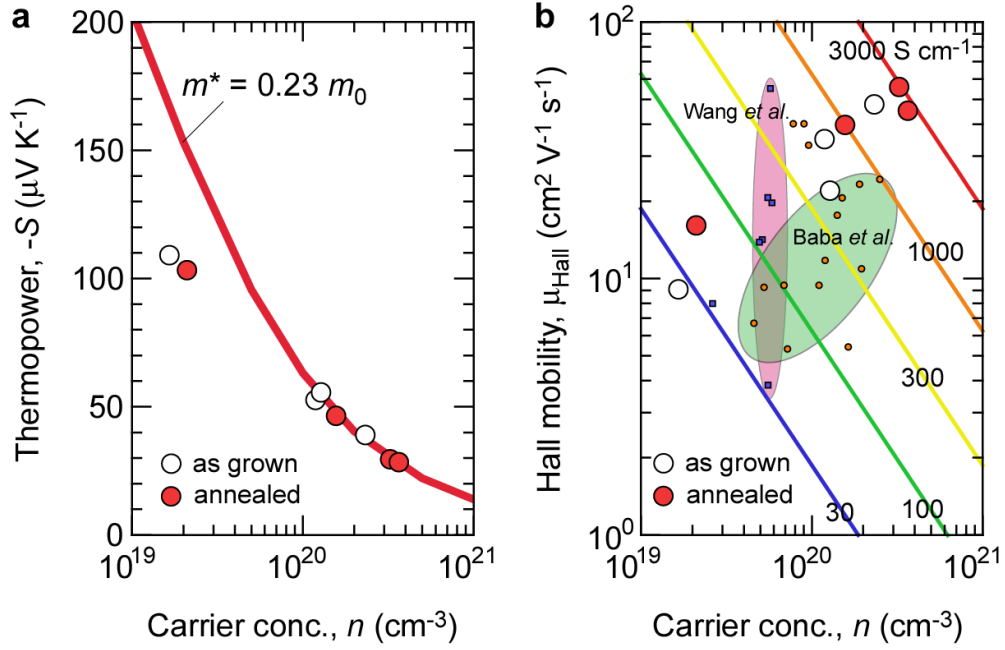
Figure 5.4 (a) Thermopower (−*S*) and (b) Hall mobility (*μ*Hall) of resultant LSSO films as a function of carrier concentration (*n*) at room temperature. The carrier effective mass (*m**) values of LSSO is 0.23 m_0, which is clarified by the thermopower measurements. By the thermal annealing in vacuum, electrical conductivity exceed 3000 S cm^{-1} in LSSO film was achieved in addition to the mobility reached value as high as 55.8 cm^2 V^{-1} s^{-1} at a carrier concentration of 3.26×10^{20} cm^{-3}. The values reported by Wang *et al*. (blue square) and Baba *et al*. (orange circle) are also plotted for comparison.
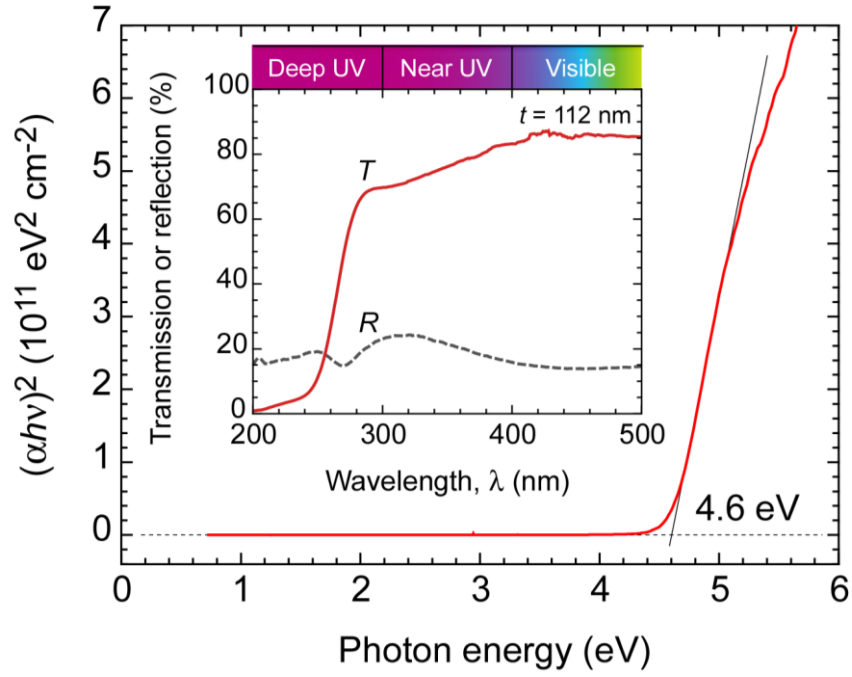
Figure 5.5 Optical bandgap of the resultant 3% La-doped LSSO thin film. The E_g was ~4.6 eV, which was obtained from the linear relationship of $(\alpha h\nu)^2$ – photon energy with assuming a direct bandgap. The absorption coefficient α was obtained from the transmission and reflection data shown in the inset.
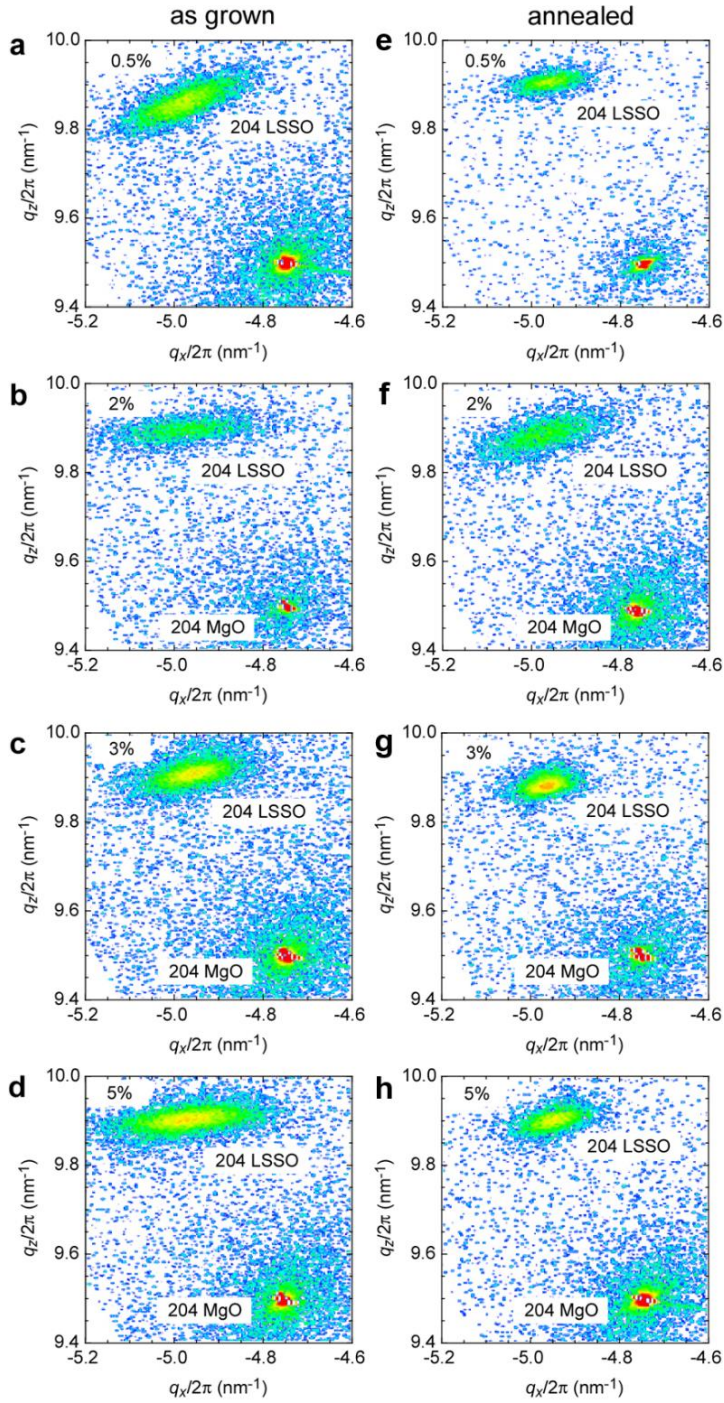
FIG. 5.6 RSM near 204 diffraction spot of the LSSO films. (a-d) as-deposited film,

(e-h) vacuum annealed at 790 °C for 30 min ($< 10^{-2}$ Pa).

6. Tuning of the Optoelectronic Properties for
Transparent Oxide Semiconductor ASnO₃
by Modulating the Size of A-ions

Chapter 6. Tuning of the Optoelectronic Properties for Transparent Oxide Semiconductor *A*SnO$_3$ by Modulating the Size of *A*-ions

6.1 Objective of this chapter

Optimizing the tradeoff relationship between optical bandgap and electrical conductivity is essential in DUV optoelectronic applications. In this regard, La-doped *A*SnO$_3$ films are interesting due to their wide bandgap and high electrical properties. As shown in previous chapters, LBSO thin films show high mobility value of 115−183 cm^2 V^{-1} s^{-1} at room temperature [37]. When a smaller Sr atom is substituted in the *A*-site, SrSnO$_3$ show E_g of ~4.6 eV allowing SrSnO$_3$-based TFT to transmit DUV light with a wavelength of 260 nm by more than 50%, which has great potential in DNA-sensing. Following this trend, if Ca, an even smaller alkaline element, occupies the *A*-site (CaSnO$_3$), further widening of the E_g value can be expected. However, the reported theoretical and experimental bandgap values of CaSnO$_3$ scattered from 1.95 to 5.38 eV [46-48].

*A*SnO$_3$ has perovskite structure composed of corner-sharing SnO$_6$ octahedra with the *A*-site cation. The crystal structure of *A*SnO$_3$ is closely related to lattice parameter which determined by *A*-site substitution. The smaller *A*-site cation with stronger binding force of nucleus trigger deformations in the SnO$_6$ octahedral and further induce phase transition

6. Tuning of the Optoelectronic Properties for
Transparent Oxide Semiconductor ASnO₃
by Modulating the Size of A-ions

in ASnO$_3$ [88]. As shown in **Figure 6.1**, BaSnO$_3$ ($a = 4.116$ Å) is cubic crystal structure with the space group $Pm\bar{3}m$. SrSnO$_3$ ($a_{pc} = 4.037$ Å) and CaSnO$_3$ ($a_{pc} = 3.954$ Å) are pseudo cubic crystal structure with the space group $Pnma$, both distorted by an octahedra tilting. Thus, the lattice parameter of ASnO$_3$ can be modulated from 3.954 to 4.116 Å by substituting the A-site. Although this system can be considered as an excellent solution to find balanced optoelectronic properties, the effect of A-site substitution on the optoelectronic properties of ASnO$_3$ has not been clarified in detail due to the lack of a systematic study.

This chapter investigates the optoelectronic properties of ASnO$_3$ in forms of solid solution systems. With increasing average ionic radius of the A-site ion, the lattice parameter almost linearly increased from 3.95 to 4.14 Å while the optical bandgap decreased from ~4.6 to ~3.6 eV. With increasing lattice parameter, the electrical conductivity gradually increased from ~10^0 to ~10^3 S cm^{-1} due to a gradual increase in both the carrier concentration and mobility. The electron transport properties of Ca-rich side solid solution films are greatly suppressed due to the large octahedral phase deformation, and La-doped CaSnO$_3$ (LCSO) showed an insulating behavior. On the other hand, LSSO exhibited a great balance between bandgap and electrical performance, which makes it a suitable ASnO$_3$ system for advanced optoelectronic applications.

6. Tuning of the Optoelectronic Properties for
Transparent Oxide Semiconductor ASnO₃
by Modulating the Size of A-ions

6.2 Experimental

3% La-doped ASnO₃ solid solution epitaxial films were fabricated on (001) LaAlO₃ (a = 3.821 Å) single crystal substrates by PLD. 3% La-doped ASnO₃ single phase ceramics were used as the PLD targets. During the film growth, the substrate temperature and oxygen pressure inside the chamber were kept at 750 °C and 20 Pa, respectively. In order to relax the lattice strain caused by the mismatch between film and substate, the thickness of all films was chosen to be ~200 nm. The X-ray RSMs were recorded to clarify the change of the lateral (in-plane) coherence lendgth (D) evaluated from the diffraction spots using Scherrer equation. A spectrophotometer (solidspec-3700, Shimazu Co.) was used to collect ultraviolet-visible (UV-vis) diffuse reflectance data in 200−1700 nm wavelength range. The optical bandgap ($E_{\text{g opt}}$) was calculated using the Tauc plot, $(\alpha h v)^2 = C (h v – E_g)$.

6.3 Results and Discussion

According to the XRD results, all the resultant films were heteroepitaxially grown on (001) LaAlO₃ substrate. The RSM of the resultant films was used to extract the lattice parameters perpendicular to the substrate surface (c-axis) and along the substrate surface (a-axis). In order to directly compare the lattice parameter of the films, the average values of $(a \cdot c)^{1/3}$ was used. **Figure 6.2** shows change in the $(a \cdot c)^{1/3}$ with A-site ion substitution. Almost linear increase of lattice parameter was observed as a function of x in

6. Tuning of the Optoelectronic Properties for
Transparent Oxide Semiconductor ASnO₃
by Modulating the Size of A-ions

$Ca_{1-x}Sr_xSnO_3$, $Sr_{1-x}Ba_xSnO_3$, and $Ba_{1-x}Ca_xSnO_3$, confirming that ionic radii of the A-site ion dominate the lattice parameter. The lateral coherence length (D) of the ASnO₃ films was also calculated. Although the average lattice parameters of the ASnO₃ films are different from each other, the D values are in the range of 20−30 nm, and there is no clear tendency observed with respect to the lattice parameter.

The optical transmission and reflection spectra of the resultant films were measured to calculate the absorption coefficient α as $\alpha = -[\ln (T + R)] \cdot t^{-1}$, where T, R, and t are transmission, reflection, and thickness, respectively. **Figure 6.3** shows the $E_{g\ opt}$ of the resultant films as a function of average lattice parameter, which gradually decreased from 4.64 eV (CaSnO₃) to 3.59 eV (BaSnO₃) with increasing the lattice parameter. By adjusting the composition of the solid solution, the E_g of ASnO₃ can easily be modulated. This is attributed to the interaction between O 2p and Sn 5s orbitals, which consist the VBM and CBM of ASnO₃ respectively. The location of the CBM and VBM are affected by the Sn–O bond length. When the distance between two adjacent Sn^{4+} and O^{2-} becomes shorter, the energy splitting between the antibonding state (=CBM) and bonding state (VBM) becomes greater. Therefore, the optical bandgap decreased with increasing the lattice parameter.

Figure 6.4 summarizes room temperature electron transport properties of the La-doped $Ca_{1-x}Sr_xSnO_3$, $Sr_{1-x}Ba_xSnO_3$, and $Ca_{1-x}Ba_xSnO_3$ solid solution films as a function of the

average lattice parameter. The σ increases more than three orders of magnitude from ~0.5 to 2240 S cm^{-1} with increasing the average lattice parameter. This is due to gradual increases in both n and μ_{Hall}, which increase gradually with the average lattice parameter. The observed n values are smaller than that of the nominal value, especially in regions of smaller lattice parameters. The absolute values of S gradually decrease with lattice parameter, which is consistent with the fact that n increases with lattice parameter. The increasing tendency of n with lattice parameter is most likely due to the reduction of the bandgap with the lattice parameter increase. Suppression of μ_{Hall} fundamentally occurs due to two reasons. One is an increase in the carrier effective mass, and the other is the reduction of relaxation time, which strongly depends on the crystalline quality of the material. For example, with the presence of boundaries, carrier transport is suppressed at the boundary when the carrier concentration is low. According to the relationship between S and log n, the carrier effective mass of the films were in the range from 0.2 to 0.3 m_0. Therefore, the A-site substitution does not strongly affect the carrier effective mass of the films. Thus, the small μ_{Hall} value at small lattice parameter side is mainly attributed to the reduction of carrier relaxation time.

In order to further investigate the tendency observed from the electron transport properties, temperature dependence of electrical resistivity of the films was measured (**Figure 6.5 (a)**). In La-doped $Ca_{1-x}Sr_xSnO_3$ and $Sr_{1-x}Ba_xSnO_3$ films, when lattice parameter is shorter than 3.97 Å, the ASnO₃ films showed an insulating behavior. On the other hand, when

6. Tuning of the Optoelectronic Properties for
Transparent Oxide Semiconductor ASnO₃
by Modulating the Size of A-ions

lattice parameter is longer than 4.01 Å, the films showed a metallic behavior. The activation energy (E_a) of the electrical conductivity around room temperature is shown in **Figure 6.5 (b)**. The E_a gradually decreased from $+22$ meV to -14 meV with increasing the average lattice parameter. These results clearly indicate that the optoelectronic properties of ASnO$_3$ can be tuned by modulating the average A-site ionic radius.

Larger A-site ion substitutions result in the decrease of the bandgap and the mobility edge; the carrier generation efficiency increases when the bandgap decreases. The carrier relaxation time increases when the mobility edge decreases. Thus, the electrical conductivity increases when larger ion is substituted in the A-site.

6.4 Conclusions

This chapter systematically investigated the optoelectronic properties of ASnO$_3$ epitaxial films on (001) LaAlO$_3$ substrates and demonstrated that ionic radius of A-site ion can be used to modulate the optoelectronic properties of ASnO$_3$. The lattice parameter can be controlled almost linearly from 3.95 to 4.14 Å with increasing the average ionic radius of the A-site ion from 1.34 (Ca^{2+}) to 1.61 Å (Ba^{2+}) while the optical bandgap gradually decreased from ~4.6 to ~3.6 eV with a small positive bowing. The electrical conductivity gradually increased from ~10^0 to ~10^3 S cm^{-1} due to a gradual increase in both the carrier concentration and mobility when the lattice parameter increased. The present results are

6. Tuning of the Optoelectronic Properties for
Transparent Oxide Semiconductor ASnO₃
by Modulating the Size of A-ions

of significant importance for designing ASnO$_3$ material system in future transparent

electronic devices.

6. Tuning of the Optoelectronic Properties for
Transparent Oxide Semiconductor ASnO₃
by Modulating the Size of A-ions

Table 6.1 Electrical and optical properties of the La-doped ASnO₃ (A = Ca, Sr, Ba) films.

A-site ion	n (10^{19} cm^{-3})	μ_{Hall} (cm^2 V^{-1} s^{-1})	σ (S cm^{-1})	E_g (eV)
Ca^{2+}	–	–	–	4.64
Sr^{2+}	23	51	1900	4.43
Ba^{2+}	22	64	2235	3.59

6. Tuning of the Optoelectronic Properties for
Transparent Oxide Semiconductor ASnO₃
by Modulating the Size of A-ions
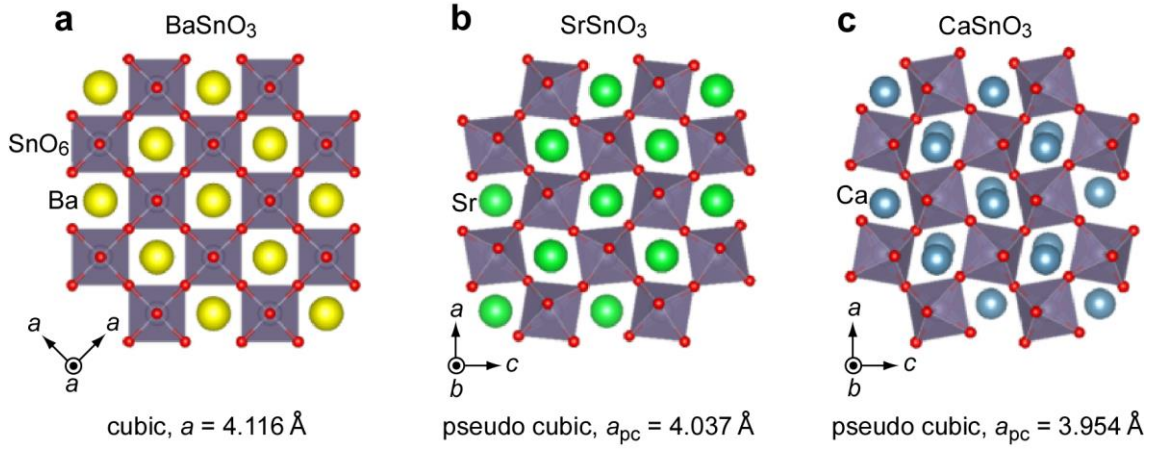
Figure 6.1 Schematic crystal structure of (a) BaSnO₃ (b) SrSnO₃ and (c) CaSnO₃. Crystal structures were obtained from the Rietveld refinement of the powder XRD patterns. ASnO₃ is consisted of layers of SnO₆ octahedra separated by A atoms. BaSnO₃ ($a = 4.116$ Å) is cubic crystal structure with the space group *Pm*-3*m*, SrSnO₃ ($a_{pc} = 4.037$ Å) and CaSnO₃ ($a_{pc} = 3.954$ Å) are orthorhombic crystal structure with the space group *Pnma*. The Shannon's ionic radius of Ca²⁺ is 1.34 Å, Sr²⁺ is 1.44 Å, and Ba²⁺ is 1.61 Å, respectively, when the coordination number is 12.

6. Tuning of the Optoelectronic Properties for
Transparent Oxide Semiconductor ASnO₃
by Modulating the Size of A-ions
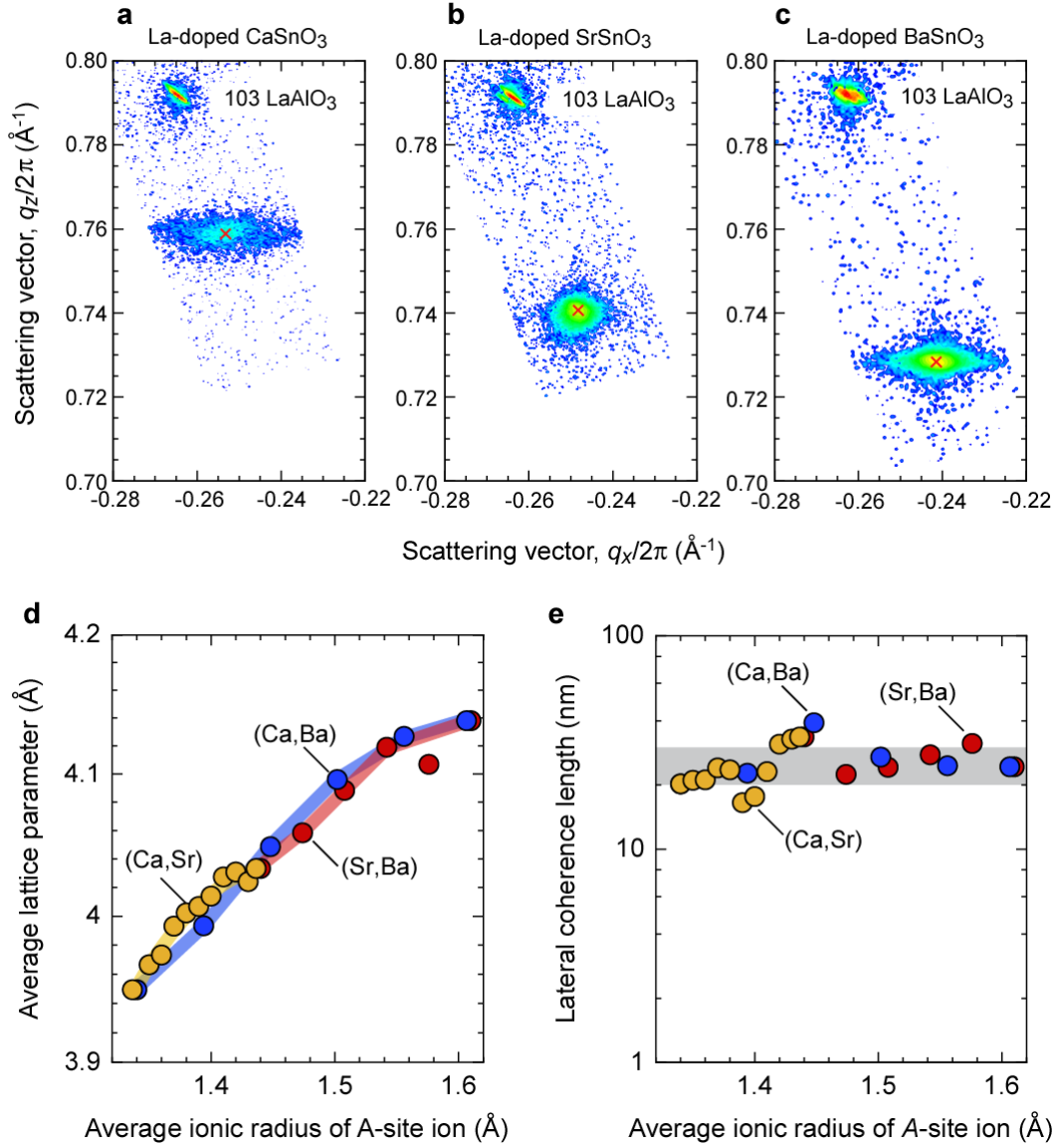
Figure 6.2 Crystallographic analyses of the *A*SnO₃ films grown on (001) LaAlO₃ substrates. (a−c) RSMs of La-doped (a) CaSnO₃, (b) SrSnO₃, and (c) BaSnO₃. Red × symbol indicates the peak position of the diffraction spot of 103 *A*SnO₃. (d) Relationship between average lattice parameter and average ionic radius of *A*-site ion in *A*SnO₃. Solid line indicates the fitted curve. (e) Lateral coherence length of the *A*SnO₃ films plotted as a function of average ionic radius of *A*-site ion. The lateral coherence length is ranging around 20−30 nm and independent from the average ionic radius.

*6. Tuning of the Optoelectronic Properties for
Transparent Oxide Semiconductor ASnO₃
by Modulating the Size of A-ions*
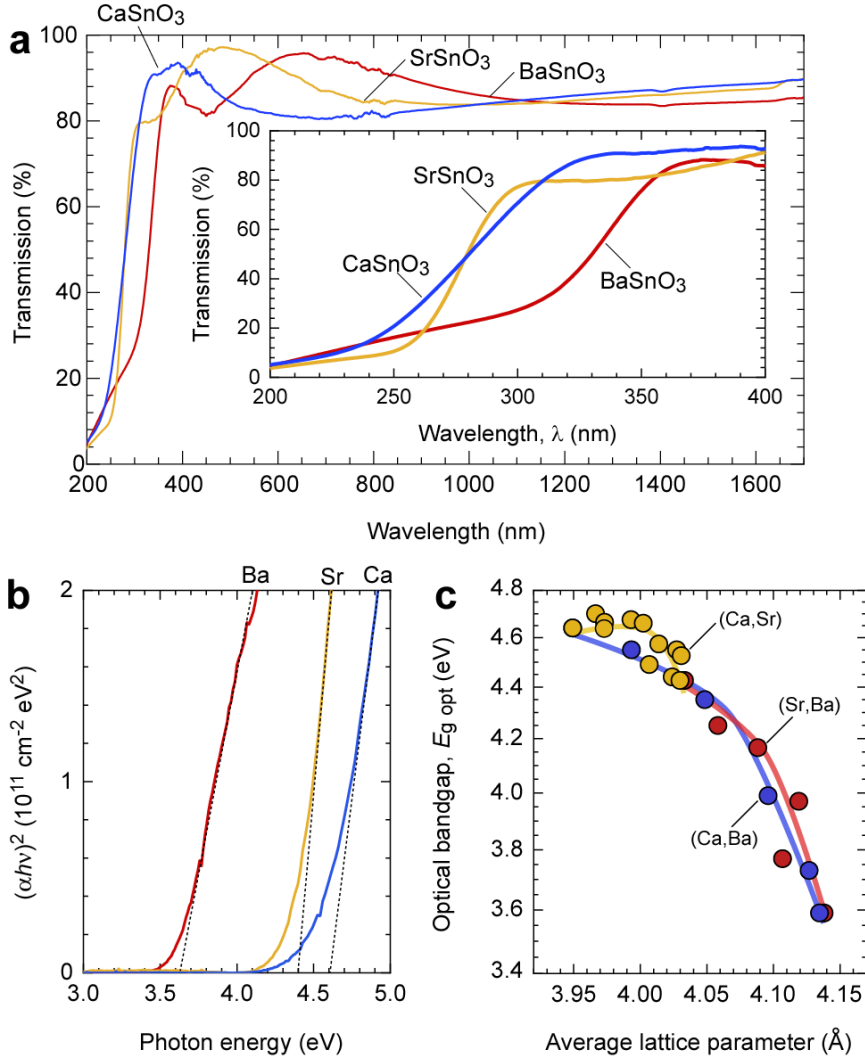
Figure 6.3 Optical properties of the *A*SnO₃ films. (a) Optical transmission spectra of the *A*SnO₃ films. The film thickness was ~100 nm. The inset shows the magnified spectra around DUV region. (b) $(\alpha h\upsilon)^2 - h\upsilon$ plots. (c) Optical bandgap (E_g) plotted as a function of average lattice parameter. E_g gradually decreases with increasing lattice parameter. The E_g of the La-doped CaSnO₃, SrSnO₃, and BaSnO₃ films are 4.64, 4.43, and 3.59 eV, respectively.

*6. Tuning of the Optoelectronic Properties for
Transparent Oxide Semiconductor ASnO₃
by Modulating the Size of A-ions*
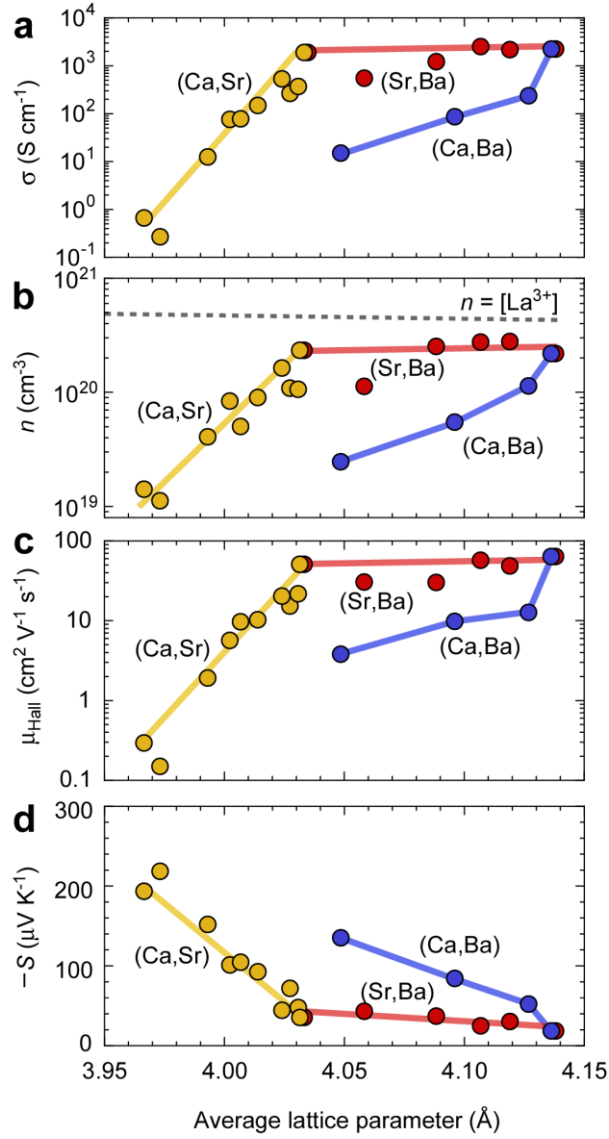
**Figure 6.4 Room temperature electron transport properties of the La-doped Ca$_{1-x}$Sr$_x$SnO$_3$, Sr$_{1-x}$Ba$_x$SnO$_3$ and Ca$_{1-x}$Ba$_x$SnO$_3$ solid solution films as a function of average lattice parameter.** (a) Electrical conductivity (σ). (b) Carrier concentration (n). (c) Hall mobility (μ_{Hall}). (d) Thermopower (S). The solid lines are the guide-to-eyes. The dotted line in (b) indicates n when doped La is fully activated. Both n and μ_{Hall} gradually increase with increasing the lattice parameter. Therefore, σ increases with lattice parameter. The increasing tendency of n is confirmed by the decreasing tendency of $-S$.
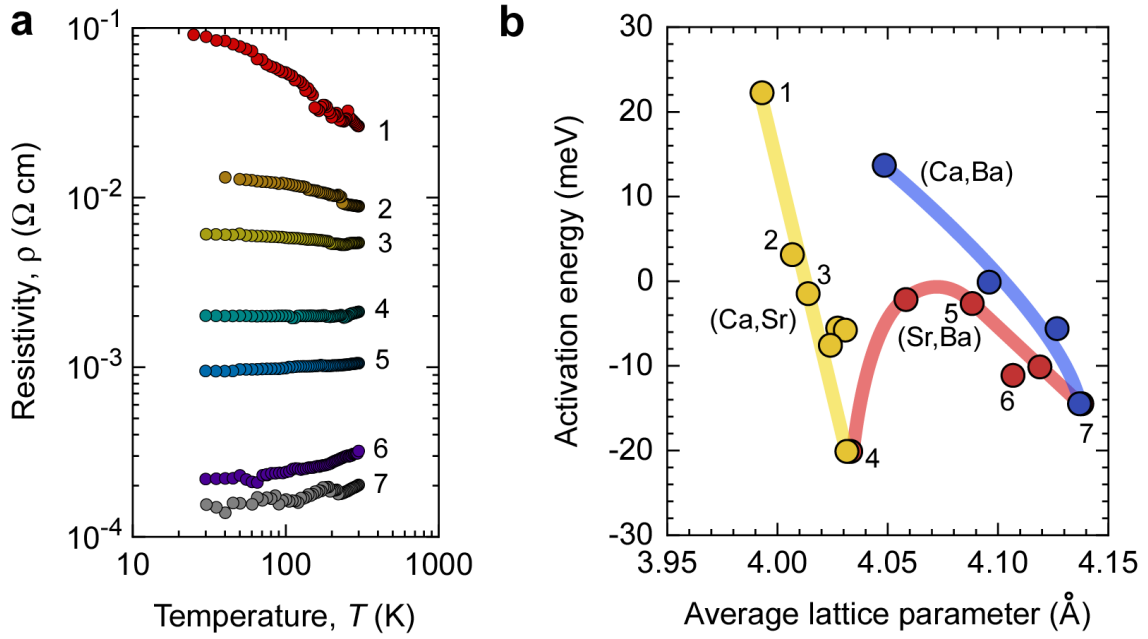
Figure 6.5 Activation energy of the electrical conductivity. (a) Temperature dependence of the electrical resistivity of the $A\mathrm{SnO_3}$ films with various lattice parameters. (b) Activation energy of the electrical conductivity (E_a), which was calculated using the Arrhenius plot.

Chapter 7. Summary and Recommendations for Future Work

The given doctoral research addressed the fundamental optoelectronic properties of perovskite ASnO$_3$ system. The potential of this material system was examined in various optoelectronic applications including high-speed TFTs (LBSO), DUV-transparent biosensors (LSSO), and wide-bandgap semiconductors (LCSO).

Chapter 3 reported that the carrier mobility of LBSO films on (001) SrTiO$_3$ and (001) MgO substrates strongly depends on the thickness without any noticeable effects from the film/substrate lattice mismatch (+5.4 % for SrTiO$_3$, −2.3 % for MgO). The films on SrTiO$_3$ and MgO substrates exhibited large structural differences including the threading dislocation densities. However, the mobility dependences on the film thickness in both cases were almost the same, saturating at ~100 cm^2 V^{-1} s^{-1} while the charge carrier densities approached the nominal carrier concentration (=[2 % La^{3+}]). This clearly indicates that the carrier mobility in LBSO films strongly depends on the thickness. Previous studies mostly focused on eliminating threading dislocations for improving the mobility of LBSO films, but this chapter showed that other factors also have to be considered thoroughly.

The presence of Sn2+ states in LBSO films lead to a hypothesis: the mobility of LBSO

films near the film/substrate interface is suppressed due to oxygen deficiency, which forms a buffered region. Therefore, in chapter 4, the buffered region in LBSO films with low electron mobility was eliminated by growing the films under highly oxidative ozone (O_3) atmospheres. The O_3 environments relaxed the LBSO lattice and reduced the formation of Sn^{2+} states, which are known to suppress the electron mobility in LBSO. The resultant O_3-LBSO films showed improved mobility values up to 115 $cm^2\ V^{-1}\ s^{-1}$, which is among the highest in LBSO films on $SrTiO_3$ substrates and comparable to LBSO films with buffer layers.

Investigation of the optoelectronic properties of ASnO$_3$ extended to LSSO, which is known as one of DUV-TCOs with an energy bandgap of ~4.6 eV. As such, LSSO has an excellent potential as a DUV-transparent electrode. However, the reported electrical conductivities of LSSO films are below 1000 $S\ cm^{-1}$, most likely due to the low activation solubility of La dapont in the LSSO lattice. Therefore, chapter 5 demonstrated that highly conducting (>3000 $S\ cm^{-1}$) LSSO thin films with an energy bandgap of ~4.6 eV can be fabricated by PLD on MgO substrate if a simple post annealing in vacuum is implemented. From the XRD and the STEM analyses, it was found that lateral grain growth occurred during the annealing, which improved the activation rate of La ion, leading to a significant improvement of carrier concentration ($3.26 \times 10^{20}\ cm^{-3}$) and Hall mobility (55.8 $cm^2\ V^{-1}\ s^{-1}$). This showed that LSSO would be useful as a DUV-transparent electrode for advanced optoelectronic devices.

Chapter 6 showed that the optoelectronic properties of ASnO$_3$ can be tuned systematically by changing the average size of A-site ions. According to the structural characteristics, the optical absorption spectra, and the electron transport properties of the ASnO$_3$ films, the lattice parameter almost increased linearly from 3.95 to 4.14 Å with increasing the average ionic radii of the A-site ion from 1.34 (Ca^{2+}) to 1.61 Å (Ba^{2+}). The optical bandgap gradually decreased from ~4.6 to ~3.6 eV with a small positive bowing. The electrical conductivity gradually increased from ~10^0 to ~10^3 S cm^{-1} due to gradual increase of both carrier concentration and mobility with increasing the lattice parameter. This chapter systematically demonstrated the overall trade-off relationship between the optical bandgap and the electrical transport properties in ASnO$_3$.

This doctoral research addressed all essential optoelectronic properties of ASnO$_3$ perovskites in both fundamental science and engineering perspectives. The fundamental characteristics of perovskite stannates associated with the optoelectronic properties found in this doctoral research will be of significant value in their utilizations in future device applications.

While this doctoral research addressed the all important optoelectronic properties of ASnO$_3$ perovskite systems, the commercialization of devices always down to the economic and technical viability. For example, high-quality epitaxial ASnO$_3$ films grow

requires single-crystal substrates and high fabrication temperatures. In this regard, technologies associated with cost reduction such as film transfer [89-92] can be considered in future. Since the given research showed that post-treating process is an effective tool for enhancing the functional properties of ASnO$_3$ films, utilizing a low-cost fabrication tool that allows large-area deposition (*i.e.,* sputtering, chemical vapor deposition) can be of value for examining the feasibility of mass production. The versatility in the optoelectronic properties of ASnO$_3$ system can also be considered in other functional applications. For example, since the electrical properties of LBSO strongly depends on the oxygen deficiency (chapter 4), electrochemical redox process [93] can be implemented in LBSO films for memory application. Further investigations in the fundamental transport characteristics will also be important. For instance, the interface between ASnO$_3$ films and substrates needs to be examined in more details with an emphasis on the electron transport mechanism to reduce the film thicknesses in devices. Dopants other than La can also be of interest in research community, especially for CaSnO$_3$ since no conducting CaSnO$_3$ film was reported to date.

References

[1] Chen, Janglin, Wayne Cranton, and Mark Fihn, eds. *Handbook of visual display technology*. Berlin, Germany: Springer, 2016.

[2] Akasaki, Isamu, Hiroshi Amano, and Shuji Nakamura. "Blue LEDs–Filling the world with new light." *The Royal Swedish Academy of Sciences-The Nobel Prize in Physics* (2014).

[3] Ohta, Hiromichi, and Hideo Hosono. "Transparent oxide optoelectronics." *Materials Today* 7.6 (2004): 42-51.

[4] Gordon, Roy G. "Criteria for choosing transparent conductors." *MRS bulletin* 25.8 (2000): 52-57.

[5] Ohta, Hiromichi, *et al.* "Highly electrically conductive indium–tin–oxide thin films epitaxially grown on yttria-stabilized zirconia (100) by pulsed-laser deposition." *Applied Physics Letters* 76.19 (2000): 2740-2742.

[6] Haxel, Gordon. *Rare earth elements: critical resources for high technology*. Vol. 87. No. 2. US Department of the Interior, US Geological Survey, 2002.

[7] Kamiya, Toshio, and Hideo Hosono. "Material characteristics and applications of transparent amorphous oxide semiconductors." *NPG Asia Materials* 2.1 (2010): 15-22.

[8] Nomura, Kenji, *et al.* "Room-temperature fabrication of transparent flexible thin-film transistors using amorphous oxide semiconductors." *Nature* 432.7016 (2004): 488-492.

[9] Orita, Masahiro, *et al.* "Amorphous transparent conductive oxide $InGaO_3(ZnO)_m$ (m$\leq$ 4): a Zn4s conductor." *Philosophical magazine B* 81.5 (2001): 501-515.

[10] Minami, Tadatsugu. "Substitution of transparent conducting oxide thin films for indium tin oxide transparent electrode applications." *Thin solid films* 516.7 (2008): 1314-1321.

[11] Yamamoto, Tetsuya, *et al.* "Ga-doped zinc oxide: An attractive potential substitute for ITO, large-area coating, and control of electrical and optical properties on glass and polymer substrates." *Journal of the Society for Information Display* 16.7 (2008): 713-719.

[12] Dattoli, Eric N., *et al.* "Fully transparent thin-film transistor devices based on SnO_2 nanowires." *Nano letters* 7.8 (2007): 2463-2469.

[13] Shih, Chen Wei, *et al.* "Remarkably high mobility ultra-thin-film metal-oxide transistor with strongly overlapped orbitals." *Scientific reports* 6.1 (2016): 1-6.

[14] Kim, Won-Sik, Sung Bo Lee, and Seong-Hyeon Hong. "Gas sensing properties in epitaxial SnO_2 films grown on TiO_2 single crystals with various orientations." *Sensors and Actuators B: Chemical* 147.2 (2010): 653-659.

[15] Lantto, Vilho, Tapio T. Rantala, and Tuomo S. Rantala. "Atomistic understanding of semiconductor gas sensors." *Journal of the European Ceramic Society* 21.10-11 (2001): 1961-1965.

[16] Hosono, Hideo. "Recent progress in transparent oxide semiconductors: Materials and device application." *Thin solid films* 515.15 (2007): 6000-6014.

[17] Kim, Jayoung, *et al.* "Wearable biosensors for healthcare monitoring." *Nature biotechnology* 37.4 (2019): 389-406.

[18] Yang, Yiran, and Wei Gao. "Wearable and flexible electronics for continuous molecular monitoring." *Chemical Society Reviews* 48.6 (2019): 1465-1491.

[19] Zhang, Ziyi, *et al.* "A 271.8 nm deep-ultraviolet laser diode for room temperature operation." *Applied Physics Express* 12.12 (2019): 124003.

[20] Orita, Masahiro, *et al.* "Deep-ultraviolet transparent conductive β-Ga_2O_3 thin films." *Applied Physics Letters* 77.25 (2000): 4166-4168.

[21] Wakabayashi, Ryo, *et al.* "Epitaxial structure and electronic property of β-Ga_2O_3 films grown on MgO (100) substrates by pulsed-laser deposition." *Applied Physics Letters* 111.16 (2017): 162101.

[22] Ito, Hiroshi, Kentaro Kaneko, and Shizuo Fujita. "Growth and band gap control of corundum-structured α-$(AlGa)_2O_3$ thin films on sapphire by spray-assisted mist chemical vapor deposition." *Japanese Journal of Applied Physics* 51.10R (2012): 100207.

[23] Miyakawa, Masashi, *et al.* "Fabrication of highly conductive $12CaO \cdot 7Al_2O_3$ thin films encaging hydride ions by proton implantation." *Advanced materials* 15.13 (2003): 1100-1103.

[24] Matsuishi, Satoru, *et al.* "High-density electron anions in a nanoporous single crystal: $[Ca_{24}Al_{28}O_{64}]^{4+}$(4e-)." *Science* 301.5633 (2003): 626-629.

[25] Hayashi, Katsuro, *et al.* "Light-induced conversion of an insulating refractory oxide into a persistent electronic conductor." *Nature* 419.6906 (2002): 462-465.

[26] Matsuzaki, Kosuke, *et al.* "Field-induced current modulation in epitaxial film of deep-ultraviolet transparent oxide semiconductor Ga_2O_3." *Applied physics letters* 88.9 (2006): 092106.

[27] Higashiwaki, Masataka, *et al.* "Gallium oxide (Ga_2O_3) metal-semiconductor field-effect transistors on single-crystal β-Ga_2O_3 (010) substrates." *Applied Physics Letters* 100.1 (2012): 013504.

[28] Varley, Joel B., *et al.* "Oxygen vacancies and donor impurities in β-Ga_2O_3." *Applied Physics Letters* 97.14 (2010): 142106.

[29] Walukiewicz, W. "Intrinsic limitations to the doping of wide-gap semiconductors." *Physica B: Condensed Matter* 302 (2001): 123-134.

[30] Víllora, Encarnación G., *et al.* "Electrical conductivity and carrier concentration control in β-Ga_2O_3 by Si doping." *Applied Physics Letters* 92.20 (2008): 202120.

[31] Fan, M. M., *et al.* "High-performance solar-blind ultraviolet photodetector based on mixed-phase ZnMgO thin film." *Applied Physics Letters* 105.1 (2014): 011117.

[32] Zhao, Yanmin, *et al.* "Ultraviolet photodetector based on a MgZnO film grown by radio-frequency magnetron sputtering." *ACS applied materials & interfaces* 1.11 (2009): 2428-2430.

[33] Du, Xiaolong, *et al.* "Controlled growth of high-quality ZnO-based films and fabrication of visible-blind and solar-blind ultra-violet detectors." *Advanced Materials* 21.45 (2009): 4625-4630.

[34] Zheng, Qinghong, *et al.* "MgZnO-based metal-semiconductor-metal solar-blind photodetectors on ZnO substrates." *Applied Physics Letters* 98.22 (2011): 221112.

[35] Zhang, Dan, *et al.* "A Strategy of Transparent Conductive Oxide for UV Focal Plane Array Detector: Two-Step Thermodynamic Process." *Advanced Electronic Material* 2.11 (2016): 1600320.

[36] Kim, Hyung Joon, *et al.* "Physical properties of transparent perovskite oxides (Ba, La)SnO_3 with high electrical mobility at room temperature." *Physical Review B* 86.16 (2012): 165205.

[37] Paik, Hanjong, *et al.* "Adsorption-controlled growth of La-doped $BaSnO_3$ by molecular-beam epitaxy." *Apl Materials* 5.11 (2017): 116107.

[38] Raghavan, Santosh, *et al.* "High-mobility $BaSnO_3$ grown by oxide molecular beam

epitaxy." *Apl Materials* 4.1 (2016): 016106.

[39] Lebens-Higgins, Z., *et al.* "Direct observation of electrostatically driven band gap renormalization in a degenerate perovskite transparent conducting oxide." *Physical review letters* 116.2 (2016): 027602.

[40] Wadekar, P. V., *et al.* "Improved electrical mobility in highly epitaxial La: $BaSnO_3$ films on $SmScO_3$ (110) substrates." *Applied Physics Letters* 105.5 (2014): 052104.

[41] Singh, David J., Qiang Xu, and Khuong P. Ong. "Strain effects on the band gap and optical properties of perovskite $SrSnO_3$ and $BaSnO_3$." *Applied Physics Letters* 104.1 (2014): 011910.

[42] Mizoguchi, Hiroshi, Hank W. Eng, and Patrick M. Woodward. "Probing the electronic structures of ternary perovskite and pyrochlore oxides containing Sn^{4+} or Sb^{5+}." *Inorganic chemistry* 43.5 (2004): 1667-1680.

[43] Liu, Qinzhuang, *et al.* "Ta doped $SrSnO_3$ epitaxial films as transparent conductive oxide." *Journal of Alloys and Compounds* 717 (2017): 62-68.

[44] Gao, Qiang, *et al.* "Band gap engineering and room-temperature ferromagnetism by oxygen vacancies in $SrSnO_3$ epitaxial films." *ACS applied materials & interfaces* 10.32 (2018): 27503-27509.

[45] Baba, Erina, *et al.* "Optical and transport properties of transparent conducting La-doped $SrSnO_3$ thin films." *Journal of Physics D: Applied Physics* 48.45 (2015): 455106.

[46] Henriques, J. M., *et al.* "Structural, electronic, and optical absorption properties of orthorhombic $CaSnO_3$ through ab initio calculations." *Journal of Physics: Condensed Matter* 19.10 (2007): 106214.

[47] Zhang, Weifeng, Junwang Tang, and Jinhua Ye. "Structural, photocatalytic, and photophysical properties of perovskite $MSnO_3$ (M= Ca, Sr, and Ba) photocatalysts." *Journal of materials research* 22.7 (2007): 1859-1871.

[48] Liu, Qinzhuang, *et al.* "Structure and band gap energy of $CaSnO_3$ epitaxial films on $LaAlO_3$ substrate." *Journal of Alloys and Compounds* 717 (2017): 55-61.

[49] Cherrad, Djellal, *et al.* "Ultra soft pseudo potential investigation of fundamental physical properties of $CaXO_3$ (X= Sn and Hf) distorted perovskites: A reference study to the perfect perovskites." *Physica B: Condensed Matter* 429 (2013): 95-105.

[50] Krebs, Hans-Ulrich, *et al.* "Pulsed laser deposition (PLD)--a versatile thin film

technique." *Advances in Solid State Physics*. Springer, Berlin, Heidelberg, 2003. 505-518.

[51] Chrisey, Douglas B., and Graham K. Hubler, eds. "Pulsed laser deposition of thin films." (1994): 3.

[52] Khosroshahi, Mohammad E. *Applications of biophotonics and nanobiomaterials in biomedical engineering*. CRC Press, 2017.

[53] Warren, Bertram Eugene. *X-ray Diffraction*. Courier Corporation, 1990.

[54] Huang, T. C., R. Gilles, and G. Will. "Thin-film thickness and density determination from X-ray reflectivity data using a conventional power diffractometer." *Thin Solid Films* 230.2 (1993): 99-101.

[55] Fewster, Paul F. "Reciprocal space mapping." *Critical Reviews in Solid State and Material Sciences* 22.2 (1997): 69-110.

[56] Sanchela, Anup V., *et al.* "Thermopower modulation clarification of the intrinsic effective mass in transparent oxide semiconductor $BaSnO_3$." *Physical Review Materials* 1.3 (2017): 034603.

[57] Krishnaswamy, Karthik, *et al.* "First-principles analysis of electron transport in $BaSnO_3$." *Physical Review B* 95.20 (2017): 205202.

[58] Niedermeier, Christian A., *et al.* "Solid phase epitaxial growth of high mobility La: $BaSnO_3$ thin films co-doped with interstitial hydrogen." *Applied Physics Letters* 108.17 (2016): 172101.

[59] Ganguly, Koustav, *et al.* "Structure and transport in high pressure oxygen sputter-deposited $BaSnO_{3-\delta}$." *APL materials* 3.6 (2015): 062509.

[60] Mun, Hyosik, *et al.* "Large effects of dislocations on high mobility of epitaxial perovskite $Ba_{0.96}La_{0.04}SnO_3$ films." *Applied Physics Letters* 102.25 (2013): 252105.

[61] Kim, Useong, *et al.* "Dopant-site-dependent scattering by dislocations in epitaxial films of perovskite semiconductor $BaSnO_3$." *APL Materials* 2.5 (2014): 056107.

[62] Prakash, Abhinav, *et al.* "Adsorption-controlled growth and the influence of stoichiometry on electronic transport in hybrid molecular beam epitaxy-grown $BaSnO_3$ films." *Journal of Materials Chemistry C* 5.23 (2017): 5730-5736.

[63] Lee, Woong-Jhae, *et al.* "Transparent perovskite barium stannate with high electron mobility and thermal stability." *Annual Review of Materials Research* 47 (2017): 391-423.

[64] Ozaki, Yusuke, Daisuke Kan, and Yuichi Shimakawa. "Influence of cation off-stoichiometry on structural and transport properties of (Ba, La)SnO$_3$ epitaxial thin films grown by pulsed laser deposition." *Journal of Applied Physics* 121.21 (2017): 215304.

[65] Shiogai, Junichi, *et al.* "Improvement of electron mobility in La: BaSnO$_3$ thin films by insertion of an atomically flat insulating (Sr, Ba) SnO$_3$ buffer layer." *AIP Advances* 6.6 (2016): 065305.

[66] Uher, Ctirad, ed. *Materials aspect of thermoelectricity*. CRC press, 2016.

[67] Prakash, Abhinav, *et al.* "Wide bandgap BaSnO$_3$ films with room temperature conductivity exceeding 10^4 S cm^{-1}." *Nature communications* 8.1 (2017): 1-9.

[68] Shin, Juyeon, *et al.* "High mobility BaSnO$_3$ films and field effect transistors on non-perovskite MgO substrate." *Applied Physics Letters* 109.26 (2016): 262102.

[69] Hadjarab, B., A. Bouguelia, and M. Trari. "Optical and transport properties of lanthanum-doped stannate BaSnO$_3$." *Journal of Physics D: Applied Physics* 40.19 (2007): 5833.

[70] Snyder, G. Jeffrey, and Eric S. Toberer. "Complex thermoelectric materials." *Materials for sustainable energy: a collection of peer-reviewed research and review articles from Nature Publishing Group* (2011): 101-110.

[71] Manyakin, M. D., *et al.* "A novel approach to the electronic structure and surface composition investigations of tin-oxygen system materials by means of X-ray absorption spectroscopy combined with ab initio calculations." *Computational Materials Science* 121 (2016): 119-123.

[72] Sharma, Aditya, *et al.* "X-ray absorption spectroscopy investigations on electronic structure and luminescence properties of Eu: SnO$_2$-SnO nanocomposites." *Current Applied Physics* 16.10 (2016): 1342-1348.

[73] Nesov, S. N., *et al.* "Effect of carbon nanotubes irradiation by argon ions on the formation of SnO$_{2-x}$/MWCNTs composite." *Nuclear Instruments and Methods in Physics Research Section B: Beam Interactions with Materials and Atoms* 410 (2017): 222-229.

[74] Moreno, M. S., R. F. Egerton, and P. A. Midgley. "Differentiation of tin oxides using electron energy-loss spectroscopy." *Physical Review B* 69.23 (2004): 233304.

[75] Xiang, Limin, *et al.* "Gate-controlled conductance switching in DNA." *Nature communications* 8.1 (2017): 1-10.

[76] Yamamoto, Y., *et al.* "Evaluation of buffer materials for fluorine contained solid phase epitaxy of 123 films on MgO substrates." *Physica C: Superconductivity* 412 (2004): 1316-1320.

[77] Alves, M. C. F., *et al.* "Synthesis of $SrSnO_3$ thin films by pulsed laser deposition: Influence of substrate and deposition temperature." *Thin Solid Films* 519.2 (2010): 614-618.

[78] Christen, H-M., *et al.* "Semiconducting epitaxial films of metastable $SrRu_{0.5}Sn_{0.5}O_3$ grown by pulsed laser deposition." *Applied physics letters* 70.16 (1997): 2147-2149.

[79] Smith, A. J., and A. J. E. Welch. "Some mixed metal oxides of perovskite structure." *Acta Crystallographica* 13.8 (1960): 653-656.

[80] Vegas, A., *et al.* "The $ASnO_3$ (A = Ca, Sr) perovskites." *Acta Crystallographica Section B: Structural Science* 42.2 (1986): 167-172.

[81] Taurian, O. E., M. Springborg, and N. E. Christensen. "Self-consistent electronic structures of MgO and SrO." *Solid state communications* 55.4 (1985): 351-355.

[82] Yoon, Daseob, Sangbae Yu, and Junwoo Son. "Oxygen vacancy-assisted recovery process for increasing electron mobility in n-type $BaSnO_3$ epitaxial thin films." *NPG Asia Materials* 10.4 (2018): 363-371.

[83] Weston, L., *et al.* "Origins of n-type doping difficulties in perovskite stannates." *Physical Review B* 97.5 (2018): 054112.

[84] Vining, Cronin B. "A model for the high-temperature transport properties of heavily doped n-type silicon-germanium alloys." *Journal of Applied Physics* 69.1 (1991): 331-341.

[85] Wang, Tianqi, *et al.* "Defect-driven localization crossovers in MBE-grown La-doped $SrSnO_3$ films." *Physical Review Materials* 1.6 (2017): 061601.

[86] Moreira, E., *et al.* "Structural, optoelectronic, infrared and Raman spectra of orthorhombic $SrSnO_3$ from DFT calculations." *Journal of Solid State Chemistry* 184.4 (2011): 921-928.

[87] Haacke, G. "New figure of merit for transparent conductors." *Journal of Applied Physics* 47.9 (1976): 4086-4089.

[88] Mountstevens, Elizabeth H., J. Paul Attfield, and Simon AT Redfern. "Cation-size control of structural phase transitions in tin perovskites." *Journal of Physics: Condensed*

Matter 15.49 (2003): 8315.

[89] Gu, Ke, *et al.* "Simple Method to Obtain Large-Size Single-Crystalline Oxide Sheets." *Advanced Functional Materials* 30.28 (2020): 2001236.

[90] Lu, Di, *et al.* "Synthesis of freestanding single-crystal perovskite films and heterostructures by etching of sacrificial water-soluble layers." *Nature materials* 15.12 (2016): 1255-1260.

[91] Singh, Prastuti, *et al.* "Large-area crystalline $BaSnO_3$ membranes with high electron mobilities." *ACS Applied Electronic Materials* 1.7 (2019): 1269-1274.

[92] Ji, Dianxiang, *et al.* "Freestanding crystalline oxide perovskites down to the monolayer limit." *Nature* 570.7759 (2019): 87-90.

[93] Yang, Qian, *et al.* "Solid-state electrochemical redox control of the optoelectronic properties for $SrFeO_x$ thin films." *Journal of Applied Physics* 129.21 (2021): 215303.

Acknowledgments

This study was carried out under the kind guidance of Prof. Hiromichi Ohta at Research Institute for Electronic Science, Hokkaido University from October 2016 to September 2021.

First and foremost, I would like to express my deepest gratitude to my supervisor Prof. Hiromichi Ohta (RIES, Hokkaido Univ.). He is the most genius, diligent, efficient scientist I ever know. The five years study in Ohta-Lab is the luckiest decision in my life. I learned countless things from Prof. Ohta and I cannot build my system as a researcher without Prof. Ohta's guide. His broad vision and immense knowledge help me finish my study. Without his fully support and encouragement, I cannot fulfill my research works. From him, I learned as a researcher should has depth of thinking and take care of logical of results. And if there is any possibility in my further career, I could be close to him a little bit, it will be my greatest honor.

I would like to sincerely thank Prof. Tsukasa Katayama (RIES, Hokkaido Univ.), we start to work together from this April. Although it is not a long time, he fully supports my study and discuss with me. I really enjoy working with him. And his patience with student and enthusiasm for research and efficiency in work will be my precious gains.

I would also like to deeply thank Prof. Hai Jun Cho (RIES, Hokkaido Univ.) which I cannot say enough. He always patiently inspired me, provided me with numerous advice and guidance, which I really appreciate. Every talk we had benefited me a lot. I know

there is still a long way for myself to be a real scientist. His logical thinking and reflections on the research will always be the direction of my efforts.

Then, I would like to sincerely thank every committee member, Prof. Tamotsu Hashizume, Prof. Seiya Kasai, and Prof. Toshihiro Shimada. Thank you very much for taking your time! I took Prof. Hashizume's lecture when I was in the first master year. His vast fundamental knowledge storage and well-organized lecture style have derived me learn a lot. And I do remember Prof. Hashizume's warm-hearted, taking care of me as only foreign student at the lecture. I also took one lecture of Prof. Kasai during my master time at IST. His clear logic and neat style with the white laboratory coat, built my first image of researcher. And I am very glad to know that Prof. Shimada has some experience in UESTC (I got my Bachelor degree at UESTC, Chengdu). All of them helped me a lot and gave me many useful feedbacks to improve my thesis writing.

In addition, this thesis cannot be fulfilled without the help and discussion from collaborators, and I would like to sincerely acknowledge. Prof. Anup Kumar Sanchela (Currently, Assistant Professor, Pandit Deendayal Petroleum Univ.) for the film growth and electron transport properties measurements. Prof. Hyoungjeen Jeen, Mr. Joonhyuk Lee, and Ms. Gowoon Kim (Ph.D. candidate, IST, Hokkaido Univ.) from the Pusan National University for the XAS analyses. Prof. Bin Feng and Prof. Yuichi Ikuhara from University of Tokyo for TEM analyses. Greatly appreciate for all your support!

Next, I would like to give my sincere thanks to every member in Ohta-Lab for the helps during my study and life. I am sooo lucky to meet all of you. Especially, Dr. Yuqiao

Zhang (Currently, Specially appointed professor, Jiangsu Univ.). He is always reliable, giving me countless help not only research but also study-abroad life. Dr. Takaki Onozato (OB), very warmhearted, providing me so many helps from very beginning of my study in Ohta-Lab. Dr. Xi Zhang (PD, RIES, Hokkaido Univ.), grace and elegance, discussion with her inspired me so many times. Ms. Doudou Liang (Ph.D. candidate, USTB), kind and enthusiastic, I learned a lot from her excellent experimental skill. Ms. Gowoon Kim (Ph.D. candidate, IST, Hokkaido Univ.), as my only 同期, never hesitate to provide me help, and the Korean food she made is incredibly delicious. Ms. Qian Yang (Ph.D. candidate, IST, Hokkaido Univ.), very glad to meet such a cute girl and I learned a lot from her independent and strong heart. Mr. Yuzhang Wu (Ph.D. candidate, IST, Hokkaido Univ.), we work together from the master time, countless help and support from him, gratitude. Mr. Binjie Chen (Ph.D. candidate, IST, Hokkaido Univ.), he is the guy which we call in Chinese "Winner of life". He is so knowledgeable and reliable. I benefit from every discussion with him. Mr. Lizhikun Gong (Ph.D. candidate, IST, Hokkaido Univ.), his serious attitude to experiment I learned a lot. Mr. Liao Wu (Master candidate, IST, Hokkaido Univ.) and Mr. Rui Yu (Master candidate, IST, Hokkaido Univ.), their vitality everyday reminds me of youth time. Mr. Takashi Fujimoto (Master candidate, IST, Hokkaido Univ.), he willing to discuss with me and never care about my poor Japanese. Mr. Yaoming Liu (Bachelor candidate, IST, Hokkaido Univ.), talking with you always bright me.

et al.

Moreover, I greatly appreciate for the financial support during my doctor course by China Scholarship Council. I feel so warm and grateful for the protection products and other supports during this year COVID-19 provided by my motherland.

Finally, I would give my deepest thanks to my parents who always love, inspire, and support me without any conditions. They are my most solid backing.

This is the last station of my student life. When I get my bachelor degree and graduated from UESTC five years ago, I could never image today. I would like to thank the HU and UESTC, the knowledge I learned, the attitude treated study and research benefit me till now, and the exchange student program change my life. Everyone has his own life to pursue. I would like say special thanks to myself. Your every choice, every effort and persistence, step by step, bring you here. All these days, bright or dark, happy or depressed, will be cherish part of your memory. These vivid lively experiences compose you from now on and will be your own treasure until the end. During these five years, there was quite a while time I lost the confidence, question myself, feel really anxiety and miss my rhythm. There are endless knowledge of physics, materials, and science which I need to learn. What I can do is that tiny and limited. One sentence also help me a lot, said by Hu Shih, "怕什么真理无穷，进一寸有一寸的欢喜". Try my best, making every maybe tiny effort to broaden the knowledge of human and wider the margins of science. I think this is what I want to do with my whole life.

Girls, be ambitious!

Mian Wei

Sapporo

2021.8

List of Publications

Papers related to this thesis:

[1] Anup V. Sanchela*, **Mian Wei**, Haruki Zensyo, Bin Feng, Joonhyuk Lee, Gowoon Kim, Hyoungjeen Jeen, Yuichi Ikuhara, and Hiromichi Ohta*, "Large thickness dependence of the carrier mobility in a transparent oxide semiconductor, La-doped BaSnO$_3$", *Appl. Phys. Lett.* **112**, 232102 (2018). (**IF = 3.791, TC = 20 WoS**)

[2] Anup Sanchela*, **Mian Wei**, Joonhyuk Lee, Gowoon Kim, Hyoungjeen Jeen, Bin Feng, Yuichi Ikuhara, Hai Jun Cho, Hiromichi Ohta*, "Buffer layer-less fabrication of high-mobility transparent oxide semiconductor, La-doped BaSnO$_3$", *Journal of Materials Chemistry C* **7**, 5797-5802 (2019). (**IF = 7.393, TC = 9 WoS**)

[3] **Mian Wei**, Anup Sanchela, Bin Feng, Yuichi Ikuhara, Hai Jun Cho*, and Hiromichi Ohta*, "High electrical conducting deep-ultraviolet-transparent oxide semiconductor La-doped SrSnO$_3$ exceeding ~3000 S cm^{-1}", *Appl. Phys. Lett.* **116**, 022103 (2020). (**IF = 3.791, TC = 13 WoS**)

[4] **Mian Wei***, Hai Jun Cho, and Hiromichi Ohta*, "Tuning of the optoelectronic properties for transparent oxide semiconductor ASnO$_3$ by modulating the size of A-ions" *ACS Appl. Electron. Mater.* **2**, 3971 (2020) (**IF = 3.314, TC = 0 WoS**)

Other papers:

[5] Hai Jun Cho*, Takaki Onozato, **<u>Mian Wei</u>**, Anup Sanchela, and Hiromichi Ohta*, "Effects of vacuum annealing on the electron mobility of epitaxial La-doped $BaSnO_3$ films", *APL Mater.* **7**, 022507 (2019). (**IF = 5.096, TC = 14 WoS**)

[6] Anup V. Sanchela*, **<u>Mian Wei</u>**, Hai Jun Cho, and Hiromichi Ohta*, "Thermopower modulation clarification of the operating mechanism in wide bandgap $BaSnO_3-SrSnO_3$ solid-solution based thin film transistors", *Small* **15**, 1805394 (2019). (**IF = 13.281, TC = 12 WoS**)

[7] Hai Jun Cho*, Bin Feng, Takaki Onozato, **<u>Mian Wei</u>**, Anup Sanchela, Yuichi Ikuhara, and Hiromichi Ohta*, "Investigation of electrical and thermal transport property reductions in La-doped $BaSnO_3$ films", *Phys. Rev. Materials* **3**, 094601 (2019). **Editors' Suggestion** (**IF = 3.989, TC = 5 WoS**)

[8] Hai Jun Cho*, Koichi Sato, **<u>Mian Wei</u>**, Gowoon Kim, and Hiromichi Ohta*, "Effect of lattice distortions on the electron and thermal transport properties of transparent oxide semiconductor $Ba_{1-x}Sr_xSnO_3$ solid solution films", *J. Appl. Phys.* **127**, 115701 (2020). **Editors' pick (IF = 2.546, TC = 3 WoS)**

[9] **<u>Mian Wei</u>**[#], Lizhikun Gong[#], Dou-dou Liang[#], Hai Jun Cho*, and Hiromichi Ohta*, "Fabrication and Operating Mechanism of Deep-UV Transparent Semiconducting $SrSnO_3$-based Thin Film Transistor", *Adv. Electron. Mater.* **6**, 2000100 (2020). (# Equally

contributed to this work) (**IF = 7.295, TC = 1 WoS**)

List of Presentations

[1] **<u>Mian Wei</u>**, Hai Jun Cho, and Hiromichi Ohta, "Modulation of Optical and Electronical Properties for Transparent Oxide Semiconductor ASnO$_3$ by the A-site ion substitution", The 63rd Electronic Materials Conference (EMC), Online, June 23th-25th, 2021. (Oral)

[2] **<u>Mian Wei</u>**, Hai Jun Cho, and Hiromichi Ohta, "Tuning of the Optoelectronic Properties for Transparent Oxide Semiconductor ASnO$_3$ by Modulating the Size of A-ions", 8th International Congress on Ceramics (ICC8), Online, April 25th-30th, 2021. (Oral)

[3] **<u>Mian Wei</u>**, Hai Jun Cho, and Hiromichi Ohta, "Band Engineering of Transparent Oxide Semiconductor ASnO$_3$ (A = Ba, Ca, and Sr)", 2021 年 第 68 回応用物理学会春季学術講演会, Online, March 16th-19th, 2021. (Oral)

[4] **<u>Mian Wei</u>**, Hai Jun Cho, and Hiromichi Ohta, "Tuning of the Optoelectronic Properties for Transparent Oxide Semiconductor ASnO$_3$ by Modulating the Size of A-ions", 2021 年 第 56 回応用物理学会北海道支部学術講演会, Online, January 9th-10th, 2021. (Oral)

[5] **<u>Mian Wei</u>**, Anup V. Sanchela, Bin Feng, Yuichi Ikuhara, Hai Jun Cho, and Hiromichi Ohta, "New Deep-Ultraviolet Transparent Oxide Semiconductor, La-doped SrSnO$_3$", The

3rd Workshop on Functional Materials Science, Sapporo, Japan, December 18th-20th, 2019. (Poster)

[6] **Mian Wei**, Anup V. Sanchela, Hai Jun Cho, and Hiromichi Ohta, "High electrical conductivity exceeding ~3000 S cm^{-1} of a transparent oxide semiconductor, La-doped SrSnO$_3$", Materials Research Meeting 2019, Yokohama, Japan, December 10-14, 2019

[7] **Mian Wei**, Anup V. Sanchela, Bin Feng, Yuichi Ikuhara, Hai Jun Cho, and Hiromichi Ohta, "Epitaxial film growth of a deep-ultraviolet transparent oxide semiconductor, La-doped SrSnO$_3$", RIES-NCTU Workshop, Hokkaido University, Sapporo, Japan, December 3-4, 2019. (Poster)

[8] **Mian Wei**, Anup V. Sanchela, Bin Feng, Yuichi Ikuhara, Hai Jun Cho, and Hiromichi Ohta, "Epitaxial film growth of a deep-ultraviolet transparent oxide semiconductor, La-doped SrSnO$_3$", The 20th RIES-HOKUDAI International Symposium, Hokkaido University, Sapporo, Japan, December 2-3, 2019. (Poster)

[9] **Mian Wei**, Anup V. Sanchela, Bin Feng, Yuichi Ikuhara, Hai Jun Cho, and Hiromichi Ohta, "New Deep-Ultraviolet Transparent Oxide Semiconductor, La-doped SrSnO$_3$", TOEO-11, Nara, Japan, October 7-9, 2019 **Best Poster Award (Gold)**

[10] 魏 冕, Anup Sanchela, 馮 斌, 幾原雄一, Hai Jun Cho, 太田裕道, "3000 S cm^{-1} を超える高導電性深紫外透明酸化物半導体 La ドープ SrSnO$_3$", 2019 年 第 80 回応用物理学会秋季学術講演会, 北海道大学 札幌キャンパス, 北海道札幌市, 2019 年

107

9 月 18 日-21 日.

[11] **<u>Mian Wei</u>**, Anup V. Sanchela, Hai Jun Cho, Hiromichi Ohta, "Thermopower analysis of effective mass in a transparent oxide semiconductor, La-doped $SrSnO_3$", The 19th RIES-HOKUDAI International Symposium 組[So], Jozankei View Hotel, Sapporo, December 11th-12th, 2018 (Poster) **Poster Award**

[12] **<u>M. Wei</u>**, A. Sanchela, J. Lee, G. Kim, H. Jeen, B. Feng, Y. Ikuhara, H. Cho, and H. Ohta, "Electron mobility improvement of La-doped $BaSnO_3$ films grown under the ozone atmosphere", The 2nd Workshop on Functional Materials Science, Busan, South Korea, October 22-23, 2018

[13] **<u>M. Wei</u>**, A. Sanchela, J. Lee, G. Kim, H. Jeen, B. Feng, Y. Ikuhara, H. Cho and H. Ohta, "A perverse transparent oxide semiconductor, La:$BaSnO_3$", 2018 年 第 79 回 応用物理学会秋季学術講演会, 名古屋国際会議場(名古屋・愛知), 2018 年 9 月 18 日-21 日

[14] **<u>Mian Wei</u>**, Anup V. Sanchela, Bin Feng, Joonhyuk Lee, Gowoon Kim, Hyoungjeen Jeen, Yuichi Ikuhara, and Hiromichi Ohta, "Origin of Mobility Suppression in La-doped $BaSnO_3$ Films (II)", 2018 年 第 65 回応用物理学会春季学術講演会, Waseda University (Tokyo), 17-20 March, 2018 (Domestic)

[15] **<u>M. Wei</u>**, A. V. Sanchela, B.Feng, J. Lee, G. Kim, H. Jeen, Y. Ikuhara and H. Ohta, "Origin of mobility suppression in La-doped $BaSnO_3$ films", 第 53 回応用物理学会北

海道支部/第 14 回日本光学会北海道支部合同学術講演会, Hokkaido University, 6-

7 Jan. 2018 (Domestic) **Encouragement Award**

List of Awards

[1] Best Poster Award (Gold) at 11th International Symposium on Transparent Oxide and Related Materials for Electronics and Optics (TOEO-11) (October 9th, 2019). "New Deep-Ultraviolet Transparent Oxide Semiconductor, La-doped $SrSnO_3$", **Mian Wei**, Anup Sanchela, Bin Feng, Yuichi Ikuhara, Hai Jun Cho, and Hiromichi Ohta

[2] Poster Award for the Presentation in the 19th RIES-Hokudai International Symposium. (December 12th, 2018) **Mian Wei**, Anup V. Sanchela, Hai Jun Cho, Hiromichi Ohta, "Thermopower analysis of effective mass in a transparent oxide semiconductor, La-doped $SrSnO_3$", The 19th RIES-HOKUDAI International Symposium 組[So], Jozankei View Hotel, Sapporo, December 11th-12th, 2018 (Poster)

[3] Encouragement Award for Presentation in Hokkaido Branch of the Japan Society of Applied Physics, **Mian Wei**, Anup V. Sanchela, Bin Feng, Joonhyuk Lee, Gowoon Kim, Hyoungjeen Jeen, Yuichi Ikuhara, Hiromichi Ohta, "Origin of mobility suppression in La-doped $BaSnO_3$ films", The 53rd JSAP Hokkaido Branch Meeting, Hokkaido University, Sapporo, Japan, 6-7 January, 2018